FRONTIERS OF PHYSICS

RESEARCH ARTICLE
Volume 19 / Issue 3 / 33204 / 2024

Parity-dependent skin effects and topological properties in the multilayer nonreciprocal Su–Schrieffer–Heeger structures

Jia-Rui Li[1], Cui Jiang[2], Han Su[1], Di Qi[1], Lian-Lian Zhang[1], Wei-Jiang Gong[1,†]

1 College of Sciences, Northeastern University, Shenyang 110819, China
2 Basic Department, Shenyang Institute of Engineering, Shenyang 110136, China
Corresponding author. E-mail: †gwj@mail.neu.edu.cn
Received May 10, 2023; accepted September 20, 2023

ABSTRACT

We concentrate on the skin effects and topological properties in the multilayer non-Hermitian Su–Schrieffer–Heeger (SSH) structure, by taking into account the nonreciprocal couplings between the different sublattices in the unit cells. Following the detailed demonstration of the theoretical method, we find that in this system, the skin effects and topological phase transitions induced by nonreciprocal couplings display the apparent parity effect, following the increase of the layer number of this SSH structure. On the one hand, the skin effect is determined by the parity of the layer number of this SSH system, as well as the parity of the band index of the bulk states. On the other hand, for the topological edge modes, such an interesting parity effect can also be observed clearly. Next, when the parameter disorders are taken into account, the zero-energy edge modes in the odd-layer structures tend to be more robust, whereas the other edge modes are easy to be destroyed. In view of these results, it can be ascertained that the findings in this work promote to understand the influences of nonreciprocal couplings on the skin effects and topological properties in the multilayer SSH lattices.

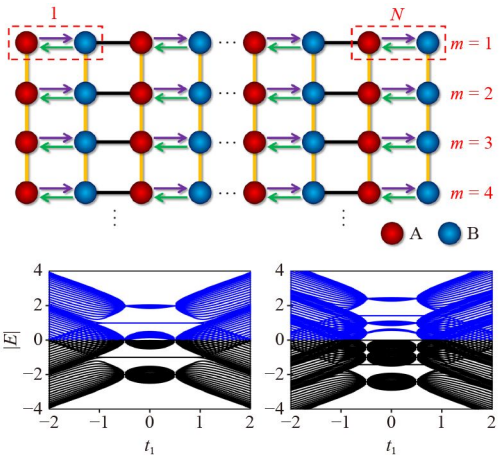

Keywords multilayer SSH lattice, nonreciprocal couplings, band structure, skin effect

1 Introduction

Non-Hermitian systems are the open structures that can be described by non-Hermitian Hamiltonians. In recent years, they have attracted great interest from both theoretical and experimental aspects [1–6]. In particular, non-Hermitian topological systems have been found to possess profound application values in enhanced sensing [7–9], topological lasers [10], and topological optical funneling [11], because of their new and interesting topological phenomena. Following the development of the relevant theory and experiment, lots of groups have demonstrated that there are two main ways to realize non-Hermitian systems: One is to use gain and loss potentials [12–15], and the other is to consider the nonreciprocal couplings [16–19].

For the systems with finite potential gain and loss, they have attracted attention since such systems can be of parity–time ($\mathcal{PT}$) symmetry. In 1998, Bender and Boettcher [20] discovered that non-Hermitian operators with $\mathcal{PT}$ symmetry are allowed to have the completely real energy spectra. This indeed promotes the development

Higher Education Press

https://doi.org/10.1007/s11467-023-1350-y

of researches on non-Hermitian systems [21]. On the experimental side, researchers have found that $\mathcal{PT}$-symmetric systems can be achieved in optics [33–36], topological circuits [37, 38], and topological photonic structures [39–42]. With further researches, $\mathcal{PT}$ symmetry has also been applied to various fields, such as single-mode lasing action in $\mathcal{PT}$-symmetric microcavity arrangements [43], achieving enhanced spin Hall effect (SHE) of light [44], metamaterials with extraordinary properties [45, 46], and perfect cavity absorber lasers [47, 48]. Following the deepening of the researches, various groups prefer to introduce $\mathcal{PT}$-symmetric imaginary potentials with gain and loss into topological systems, such as one-dimensional Su–Schrieffer–Heeger (SSH) chains, Kitaev models, trimer lattices, graphene, and two-dimensional SSH lattices [22–32], to explore the new and valuable topological phase transition manners.

The other non-Hermitian systems are those of non-reciprocal coupling terms, in which the intensity of the hopping amplitudes between the lattice points are asymmetric with each other. According to the previous reports, this characteristic causes the systems to display the non-Hermitian skin effect, that is, eigenstates with open boundary conditions (OBC) are localized near the boundary of the system in the form of exponential decay in 1D systems [49–53]. Due to the occurrence of non-Hermitian skin effect, the bulk–boundary correspondence of the system completely collapses [49, 54]. As a result, such breakdown of the bulk–boundary correspondence directly causes the topological invariants in periodic boundary conditions to be fail to describe the topological properties of the systems with non-reciprocal couplings. In 2019, Wang *et al.* [49] proposed the non-Bloch energy band theory to achieve the discussion of the topological characteristics. Related concepts have subsequently been proposed, such as generalized Brillouin zone (GBZ) [55–57], non-Bloch bulk-boundary correspondence [49], and non-Bloch topological invariants [49, 55]. At present, non-Hermitian skin effect and non-Bloch energy band theory have been realized and applied experimentally, including cold atoms, quantum optical systems, optical grid systems [58–61] and topolectrical circuit [62]. Furthermore, in photonic systems, researchers have used ring resonator arrays to explore and realize one- or two-dimensional topological photonic systems with asymmetric coupling [63].

In view of the current progress in theoretical and experimental investigations of non-reciprocal systems, we are motivated to think about more interesting phenomena by designing SSH-derived structures. In this work, we design multilayer nonreciprocal SSH structures. By considering the nonreciprocal couplings between different sublattices in the unit cells, we aim to discussion the non-Hermitian skin effects and topological properties in the multilayer non-Hermitian SSH structure. The calculation results show that the non-Hermitian skin effect due to non-reciprocal coupling exhibits the significant parity effect as the number of layers of the SSH structure increases. Namely, the skin effect is determined by the parity of the layer number of this SSH system, as well as the parity of the band index of the bulk states. In addition, the topological edge modes are also dependent on the parity of the number of layers. These results assist to understand the effect of nonreciprocal couplings on the skin effects and topological properties in multilayer SSH lattices.

2 Theory

Our considered multilayer nonreciprocal SSH structure is shown in Fig. 1(a). In this figure, the red and blue dots represent the sublattice A and B in each layer. The system Hamiltonian can be written as

$$\begin{aligned} H = &\sum_{m}\sum_{n=1}^{N}(t_{1L}a_{m,n}^{\dagger}b_{m,n} + t_{1R}b_{m,n}^{\dagger}a_{m,n}) \\ &+ \sum_{m}\sum_{n=1}^{N-1}(t_2 b_{m,n}^{\dagger}a_{m,n+1} + h.c.) \\ &+ \sum_{m}\sum_{n=1}^{N} t_3(a_{m,n}^{\dagger}a_{m+1,n} + b_{m,n}^{\dagger}b_{m+1,n} + h.c.). \end{aligned} \tag{1}$$

$\alpha_{m,n}^{\dagger}(\alpha_{m,n})$ is the creation (annihilation) operator of sublattice α ($\alpha \in a, b$) in the mth layer of the nth unit cell. N is the total number of unit cells. $t_{1L(1R)} = t_1 \pm \gamma$ represent the hopping amplitudes between the different sublattices in the unit cells, and γ denotes the nonreciprocal coupling strength, as shown by the purple and green arrow lines in Fig. 1(a). Note that the irreversible couplings between the sublattices A and B within the same cell contribute to the formation of the non-Hermitian system. Next, t_2 stands for the intercell hopping coefficient, and t_3 describes the hopping coefficient between the same kind of sublattices in one unit cell, as shown by the black and yellow lines. In terms of parameter settings, we would like to take t_1, t_2, t_3, and γ to be real numbers.

According to the expression in Eq. (1), we would like to write out the matrix form of the Hamiltonian in the real space, i.e., $H = \Psi^{\dagger}H_0\Psi$, where

$$H_0 = \begin{pmatrix} H_{m=1} & H_{12} & 0 & \cdots & 0 \\ H_{12}^{*} & H_{m=2} & H_{23} & \cdots & 0 \\ 0 & H_{23}^{*} & H_{m=3} & \ddots & \vdots \\ \vdots & \ddots & \ddots & \ddots & H_{M-1M} \\ 0 & \cdots & 0 & H_{M-1M}^{*} & H_{m=M} \end{pmatrix}, \tag{2}$$

and $\Psi = (\Psi_{m=1}, \Psi_{m=2}, \cdots, \Psi_{m=M})^{\mathrm{T}}$, with $\Psi_m = (\psi_{a,m,1},$

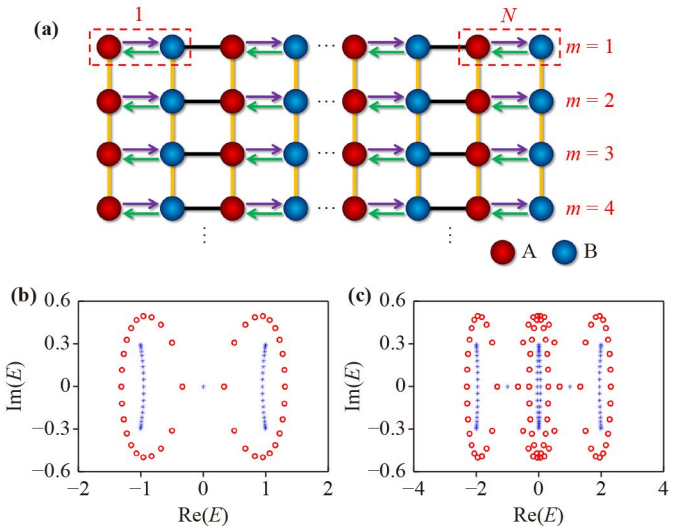

Fig. 1 **(a)** Schematic diagram of the multilayer nonreciprocal SSH structure. The red and blue dots represent the sublattices A and B. The green and purple arrow lines indicate the intracell hopping terms t_{1L} and t_{1R}, and black lines stand for the intercell hopping term t_2. In addition, the yellow lines denote the interlayer hopping coefficient t_3, and m means the number of layers. **(b, c)** Spectra of Im(E)–Re(E) in the cases of $M = 1$ and $M = 2$, respectively. The red circles and blue stars mean the spectra corresponding to the PBC and OBC cases, respectively. Other parameters are $t_1 = 0.4$, $t_2 = t_3 = 1.0$, and $\gamma = 0.5$.

$\psi_{b,m,1}, \psi_{a,m,2}, \psi_{b,m,2}, \cdots, \psi_{a,m,N}, \psi_{b,m,N})$. For the elements of H_0, they can be expressed as

$$H_m = \begin{pmatrix} 0 & t_{1L} & 0 & 0 & \cdots \\ t_{1R} & 0 & t_2 & 0 & \cdots \\ 0 & t_2 & 0 & t_{1L} & \cdots \\ 0 & 0 & t_{1R} & 0 & \cdots \\ \vdots & \vdots & \vdots & \vdots & \ddots \end{pmatrix}_{2N\times 2N},$$

$$H_{m-1,m} = \begin{pmatrix} t_3 & 0 & \cdots & 0 \\ 0 & t_3 & \ddots & 0 \\ \vdots & \ddots & \ddots & \vdots \\ 0 & \cdots & \cdots & t_3 \end{pmatrix}_{2N\times 2N}. \quad (3)$$

Since the skin effect is the intrinsic characteristic of nonreciprocal systems, our main discussion will focus on the topological phase transition in this structure. It is well known that any Hamiltonian symmetry determines the symmetry-protected topological phase with the topological structure. Therefore, we first study the topological properties of this system by discussing the symmetries. Due to the presence of nonzero γ, the system becomes non-Hermitian. Kawabata *et al.* [64] gave definitions and conditions for various symmetries of non-Hermitian systems. According to their conclusions, our system satisfies the time-reversal symmetry (TRS†), i.e., $\mathcal{T}H^{\mathrm{T}}\mathcal{T}^{-1} = H$. The TRS† operator can be expressed as $\mathcal{T} = \mathrm{off-diag}(1,1,\ldots,1)_m \otimes \mathrm{off-diag}(1,1,\ldots,1)_{2N}$ $(\mathcal{T}\mathcal{T}^* = I)$, in which

$$\mathrm{off-diag}(1,1,\ldots,1)_{m(2N)} = \begin{pmatrix} 0 & \cdots & 0 & 1 \\ 0 & \cdots & 1 & 0 \\ \vdots & \iddots & \vdots & \vdots \\ 1 & \cdots & 0 & 0 \end{pmatrix}_{m*m(2N\times 2N)}.$$

Also, this system has the particle–hole symmetry (PHS†), i.e., $\mathcal{C}H^*\mathcal{C}^{-1} = -H$ with $\mathcal{C} = \mathrm{diag}(1,-1,1,\ldots)_m \otimes \mathrm{diag}(1,-1,1,\ldots,-1)_{2N}$ $(\mathcal{C}\mathcal{C}^* = I)$. Specifically, for the case of $M = 1$, the expression of $\mathcal{C}$ operator is $\mathcal{C} = \mathrm{diag}(1,-1,1,\ldots,-1)_{2N}$, the operator of PHS† for $M = 2$ can be written as $\mathcal{C} = \mathrm{diag}(1,-1,1,\ldots,-1,-1,1,-1,\ldots,1)_{4N}$, and the operator of $M = 3$ is $\mathcal{C} = \mathrm{diag}(1,-1,\ldots,-1,-1,1,\ldots,1,1,-1,\ldots,-1)_{6N}$. The satisfaction of the particle-hole symmetry signifies that the energy eigenvalues are symmetric about energy zero point [32]. Moreover, our system satisfies the chiral symmetry, that is $\Gamma H^\dagger \Gamma^{-1} = -H$, with the operator defined as $\Gamma = \mathrm{off-diag}(1,-1,1,\ldots)_m \otimes \mathrm{off-diag}(1,-1,1,\ldots,-1)_{2N}$. The chiral symmetry operator can also be written as $\Gamma = \mathcal{T}\mathcal{C}$. The satisfaction of chiral symmetry suggests that the eigenvalues in this system appear in pairs as $(E,-E)$ [17, 49]. Accompanied by the above result, the matrix forms of TRS†, PHS† and CS symmetries in the cases of $M = 1$, $M = 2$ and $M = 3$ are given in Table 1.

Topological systems can be classified according to their symmetries [64, 65]. Thus, in order to clarify the topological properties of our system, its topological classification should be determined. The above discussion indicates that in the non-Hermitian case, it belongs to the BDI† class among the 38 topological classifications. Based on the previous works [64, 65], it can be ascertained by calculations that the real part of the energy eigenvalues is not equal to zero, except for the phase transition point, and the system has a real line gap. Now, with the help of the above analysis and the conclusions of previous works, we know that our system has a $\mathcal{Z}$-class of topological invariants.

With the help of the traditional discussion methods [66, 67], we can clarify the topological phase transition condition by solving the Hamiltonian under the periodic boundary conditions (PBC), which is well consistent with the result under the OBC. Similarly, in Figs. 1(b) and (c), we present the energy spectra of the system under two different boundary conditions, where the red circles and blue stars represent the spectra in the PBC and OBC cases, respectively. One can clearly observe that the energy spectrum in the OBC case does not correspond to the energy spectrum at the PBC case for either $M = 1$ or $M = 2$, like the discussion in the previous works [17, 49, 68, 69]. Thus, the transition conditions from topologically nontrivial and trivial regions should be solved under the same parameter conditions. Following this understand-

Table 1 Matrix forms of the TRS†, PHS†, and CS symmetries in the cases of $M=1$, $M=2$, and $M=3$, respectively. The matrix dimension of all three types of symmetric operators is equal to $d=M*2N$.

Layers	Symmetry		
	TRS†($\mathcal{T}$)	PHS†(C)	CS(Γ)
$M=1$	$\begin{pmatrix} 0 & \cdots & 0 & 1 \\ 0 & \cdots & 1 & 0 \\ \vdots & \iddots & \vdots & \vdots \\ 1 & \cdots & 0 & 0 \end{pmatrix}_{2N}$	$\begin{pmatrix} 1 & 0 & \cdots & 0 \\ 0 & -1 & \cdots & 0 \\ \vdots & \vdots & \ddots & \vdots \\ 0 & 0 & \cdots & -1 \end{pmatrix}_{2N}$	$\begin{pmatrix} 0 & \cdots & 0 & 1 \\ 0 & \cdots & -1 & 0 \\ \vdots & \iddots & \vdots & \vdots \\ -1 & \cdots & 0 & 0 \end{pmatrix}_{2N}$
$M=2$	$\begin{pmatrix} 0 & \cdots & 0 & 1 \\ 0 & \cdots & 1 & 0 \\ \vdots & \iddots & \vdots & \vdots \\ 1 & \cdots & 0 & 0 \end{pmatrix}_{4N}$	$\begin{pmatrix} 1 & 0 & & & & & & \\ 0 & -1 & 0 & & & & & \\ & \ddots & \ddots & \ddots & & & & \\ & & 0 & -1 & 0 & & & \\ & & & 0 & -1 & 0 & & \\ & & & & 0 & 1 & \ddots & \\ & & & & & \ddots & \ddots & 0 \\ & & & & & & 0 & 1 \end{pmatrix}_{4N}$	$\begin{pmatrix} & & & & & & 0 & 1 \\ & & & & & 0 & -1 & 0 \\ & & & & \iddots & \iddots & \iddots & \\ & & & 0 & -1 & 0 & & \\ & & 0 & -1 & 0 & & & \\ & \iddots & 1 & 0 & & & & \\ 0 & \iddots & \iddots & & & & & \\ 1 & 0 & & & & & & \end{pmatrix}_{4N}$
$M=3$	$\begin{pmatrix} 0 & \cdots & 0 & 1 \\ 0 & \cdots & 1 & 0 \\ \vdots & \iddots & \vdots & \vdots \\ 1 & \cdots & 0 & 0 \end{pmatrix}_{6N}$	$\begin{pmatrix} 1 & 0 & & & & & & & & & & \\ 0 & -1 & 0 & & & & & & & & & \\ & \ddots & \ddots & \ddots & & & & & & & & \\ & & 0 & -1 & 0 & & & & & & & \\ & & & 0 & -1 & 0 & & & & & & \\ & & & & 0 & 1 & 0 & & & & & \\ & & & & & \ddots & \ddots & \ddots & & & & \\ & & & & & & 0 & 1 & 0 & & & \\ & & & & & & & 0 & 1 & 0 & & \\ & & & & & & & & 0 & -1 & \ddots & \\ & & & & & & & & & \ddots & \ddots & 0 \\ & & & & & & & & & & 0 & -1 \end{pmatrix}_{6N}$	$\begin{pmatrix} & & & & & & & & & & 0 & 1 \\ & & & & & & & & & 0 & -1 & 0 \\ & & & & & & & & \iddots & \iddots & \iddots & \\ & & & & & & & 0 & -1 & 0 & & \\ & & & & & & 0 & -1 & 0 & & & \\ & & & & & 0 & 1 & 0 & & & & \\ & & & & \iddots & \iddots & \iddots & & & & & \\ & & & 0 & 1 & 0 & & & & & & \\ & & 0 & 1 & 0 & & & & & & & \\ & \iddots & -1 & 0 & & & & & & & & \\ 0 & \iddots & \iddots & & & & & & & & & \\ -1 & 0 & & & & & & & & & & \end{pmatrix}_{6N}$

ing, we perform calculations on the topological phase transition with two methods, i.e., similarity transformation and direct root finding [17, 49].

On the one hand, regarding the similarity transformation, we can describe it as follows. For the system with $2M$ sublattices, the wavefunction can be defined as $|\Psi\rangle=(\psi_{a,1,1},\psi_{b,1,1},\cdots,\psi_{b,1,N},\psi_{a,2,1},\psi_{b,2,1}\cdots,\psi_{b,2,N},\cdots,\psi_{a,M,1},\psi_{b,M,1},\cdots,\psi_{a,M,N},\psi_{b,M,N})^{\mathrm{T}}$. And then, the eigenequation $H|\Psi\rangle=E|\Psi\rangle$ can be transformed as $\bar{H}|\bar{\Psi}\rangle=E|\bar{\Psi}\rangle$, where $|\bar{\Psi}\rangle=S^{-1}|\Psi\rangle$ and $\bar{H}=S^{-1}HS$. If we assume S to be a diagonal matrix, i.e.,

$$S=\begin{pmatrix} S_1 & 0 & 0 & \cdots & 0 & 0 \\ 0 & S_2 & 0 & \cdots & 0 & 0 \\ 0 & 0 & S_3 & \cdots & 0 & 0 \\ \vdots & \vdots & \vdots & \ddots & \vdots & \vdots \\ 0 & 0 & 0 & \cdots & S_{M-1} & 0 \\ 0 & 0 & 0 & \cdots & 0 & S_M \end{pmatrix}_{M\times M}, \quad (4)$$

where $S_m=\mathrm{diag}(1,r,r,r^2,\cdots,r^{N-1},r^{N-1},r^N)$. The new Hamiltonian in the real space will be re-expressed as

$$\begin{aligned}\bar{H}=&S^{-1}HS\\ =&\begin{pmatrix} \bar{H}_1 & \bar{H}_{12} & 0 & \cdots & 0 \\ \bar{H}_{12}^* & \bar{H}_2 & \bar{H}_{23} & \cdots & 0 \\ 0 & \bar{H}_{23}^* & \bar{H}_3 & \ddots & \vdots \\ \vdots & \ddots & \ddots & \ddots & \bar{H}_{M-1M} \\ 0 & \cdots & 0 & \bar{H}_{M-1M}^* & \bar{H}_M \end{pmatrix}, \end{aligned} \quad (5)$$

with the elements being

$$\bar{H}_m=\begin{pmatrix} 0 & rt_{1L} & 0 & 0 & \cdots \\ r^{-1}t_{1R} & 0 & t_2 & 0 & \cdots \\ 0 & t_2 & 0 & rt_{1L} & \cdots \\ 0 & 0 & r^{-1}t_{1R} & 0 & \cdots \\ \vdots & \vdots & \vdots & \vdots & \ddots \end{pmatrix}_{2N\times 2N},$$

$$\bar{H}_{m,m+1}=\begin{pmatrix} t_3 & 0 & \cdots & 0 \\ 0 & t_3 & \ddots & 0 \\ \vdots & \ddots & \ddots & \vdots \\ 0 & \cdots & \cdots & t_3 \end{pmatrix}_{2N\times 2N}. \quad (6)$$

When r satisfies $r=\sqrt{|t_{1R}/t_{1L}|}$, the hopping between different sublattices in the unit cell becomes $\sqrt{|(t_1-\gamma)/(t_1+\gamma)|}$, and then, our considered non-Hermitian system is transformed into the Hermitian system. This result indicates that the bulk–boundary correspondence is satisfied in $\bar{H}$ again, and the topological phase transition conditions can be solved under the PBC. Therefore, by employing the Fourier transformation, we are allowed to transform the newly real-space Hamiltonian $\bar{H}$ into momentum space, with its expression $\bar{H}(k)$. The energy expression $\bar{E}(k)$ can thus be obtained by diagonalizing this Hamiltonian. Finally, the topological phase transition conditions of our system can be ascertained based on the energy-band expression at the boundary of the Brillouin zone.

On the other hand, for the method of direct root finding, it is to solve the topology of the model directly by ordering the roots β at E [52, 68, 69]. In the generalized Brillouin zone (GBZ), the wavevector k becomes complex. According to the conventional Bloch theorem,

the real part of the wavevector comes from the periodicity of the system, while the non-Hermitian skin effect should be attributed to the imaginary part of the complex-valued wavevector. Therefore, by means of Fourier transformation, the original non-Hermitian Hamiltonian in the real space is transformed into the momentum space. The non-Hermitian topological phase transition can be constructed by replacing the Bloch phase factor e^{ik} with β (i.e., $e^{ik} \to \beta$, $e^{-ik} \to 1/\beta$), and the value of $\beta \equiv e^{ik}$ is restricted to a ring in the complex plane. The GBZ and energy E can be obtained by solving the equation $|\beta_i(E)| = |\beta_j(E)|$, where i, j are the middle two indexes when ordering $|\beta_i(E)|$ as $|\beta_1(E)| \leq |\beta_2(E)| \leq \cdots \leq |\beta_{2N}(E)|$. Accordingly, we can plot the spectra of $|\beta(E)| - t_1$ to observe the conditions under which topological phase transitions occur in our considered structure.

Following the above demonstration, we next try to use these two methods to study the topological phase transition conditions by considering two typical cases, i.e., $M = 2$ and $M = 3$, respectively.

2.1 Case of $M = 2$

When $M = 2$, the unit cell of this system has four sublattices, i.e., $A_{1,n}$, $B_{1,n}$, $A_{2,n}$, and $B_{2,n}$. In such a case, the Hamiltonian of the system can be simplified as $H = \sum_{n=1}^{N}(t_{1L}a_{1,n}^{\dagger}b_{1,n} + t_{1R}b_{1,n}^{\dagger}a_{1,n}) + \sum_{n=1}^{N}(t_{1L}a_{2,n}^{\dagger}b_{2,n} + t_{1R}b_{2,n}^{\dagger}a_{2,n}) + \sum_{n=1}^{N-1} t_2(b_{1,n}^{\dagger}a_{1,n+1} + b_{2,n}^{\dagger}a_{2,n+1} + h.c.) + \sum_{n=1}^{N} t_3 \cdot (a_{1,n}^{\dagger}a_{2,n} + b_{1,n}^{\dagger}b_{2,n} + h.c.)$. The wavefunction can be written as $|\Psi\rangle = (\psi_{a,1,1}, \cdots, \psi_{b,1,N}, \psi_{a,2,1}, \cdots, \psi_{b,2,N})^{\mathrm{T}}$.

Firstly, we would like to use the similarity transformation method to solve the topological phase transition condition. According to the description above, the first step is to construct new eigenequations: $\bar{H}|\bar{\Psi}\rangle = E|\bar{\Psi}\rangle$, in which the Hamiltonian and wavefunction obey the forms of $\bar{H} = S^{-1}HS$ and $|\bar{\Psi}\rangle = S^{-1}|\Psi\rangle$. S satisfies a diagonal matrix with the diagonal elements $S = \mathrm{diag}(1, r, r, r^2, \cdots, r^{N-1}, r^N, 1, r, r, r^2, \cdots, r^{N-1}, r^N)$. And then, in $\bar{H}$ we have $r^{\pm 1}(t_1 \pm \gamma)$ in the region of $t_1 \pm \gamma$. In the case of $r = \sqrt{|t_{1R}/t_{1L}|} = \sqrt{|(t_1 - \gamma)/(t_1 + \gamma)|}$, the non-Hermitian structure will be Hermitian, with the respective hopping coefficients defined as

$$\tilde{t_1} = \sqrt{(t_1 - \gamma)(t_1 + \gamma)}, \quad \tilde{t_2} = t_2, \quad \tilde{t_3} = t_3. \tag{7}$$

Accordingly, $\bar{H}$ can be rewritten as $\bar{H} = \sum_{n=1}^{N} \tilde{t_1}(\bar{a}_{1,n}^{\dagger}\bar{b}_{1,n} + \bar{a}_{2,n}^{\dagger}\bar{b}_{2,n} + h.c.) + \sum_{n=1}^{N-1} t_2(\bar{b}_{1,n}^{\dagger}\bar{a}_{1,n+1} + \bar{b}_{2,n}^{\dagger}\bar{a}_{2,n+1} + h.c.) + \sum_{n=1}^{N} t_3 \cdot (\bar{a}_{1,n}^{\dagger}\bar{a}_{2,n} + \bar{b}_{1,n}^{\dagger}\bar{b}_{2,n} + h.c.)$. Its matrix form in the momentum space is

$$\bar{H}(k) = \begin{pmatrix} 0 & \tilde{t_1} + t_2 e^{-ik} & t_3 & 0 \\ \tilde{t_1} + t_2 e^{ik} & 0 & 0 & t_3 \\ t_3 & 0 & 0 & \tilde{t_1} + t_2 e^{-ik} \\ 0 & t_3 & \tilde{t_1} + t_2 e^{ik} & 0 \end{pmatrix}. \tag{8}$$

Surely, this Hamiltonian can be expanded based on the Pauli matrices, i.e., $\bar{H}(k) = (\tilde{t_1} + t_2 \cos k)(\tau_0 \otimes \sigma_x) + t_2 \sin k \cdot (\tau_0 \otimes \sigma_y) + t_3(\tau_x \otimes \sigma_0)$, where $\tau_{x,y,z}(\sigma_{x,y,z})$ are the Pauli matrices in the corresponding subspaces and $\tau_0(\sigma_0)$ are the related unit matrices. The energy-band expressions in the momentum space can be obtained by diagonalizing the Hamiltonian of Eq. (8), i.e.,

$$\bar{E}_{\pm\pm}(k) = \pm t_3 \pm \sqrt{Y_0} \tag{9}$$

with $Y_0 = \tilde{t_1}^2 + t_2^2 + 2\tilde{t_1}t_2 \cos k$. In this Hermitian case, we can find the phase transition points between topologically-trivial and -nontrivial phases at $\tilde{t_1} = t_2$, i.e.,

$$t_1 = \pm\sqrt{t_2^2 + \gamma^2}, \quad \text{or} \quad t_1 = \pm\sqrt{\gamma^2 - t_2^2}. \tag{10}$$

Herein the energy band gap is closed at $k = \pi$, and the eigenenergies are $E = \pm t_3$.

Next, we use the other method (i.e., direct root finding) to verify the topological phase transition condition. To be specific, we first transform the real-space Hamiltonian H into the momentum space by performing the Fourier transformation. And then, by changing e^{ik} to be β, the Hamiltonian of $H(\beta)$ is expressed, i.e.,

$$H(\beta) = \begin{pmatrix} 0 & t_{1L} + t_2\beta^{-1} & t_3 & 0 \\ t_{1R} + t_2\beta & 0 & 0 & t_3 \\ t_3 & 0 & 0 & t_{1L} + t_2\beta^{-1} \\ 0 & t_3 & t_{1R} + t_2\beta & 0 \end{pmatrix}. \tag{11}$$

After calculation, one can get the relationship between E and β, that is $E_{1(2)}(\beta) = \pm t_3 - \sqrt{[\beta(\gamma + t_1) + t_2](-\gamma + t_1 + \beta t_1)/\beta}$, $E_{3(4)}(\beta) = \pm t_3 + \sqrt{[\beta(\gamma + t_1) + t_2](-\gamma + t_1 + \beta t_1)/\beta}$. According to this result, we can get the roots of $E(\beta)$:

$$\beta_{1(2)}(E) = \frac{E^2 + \gamma^2 - t_1^2 + 2Et_3 + t_3^2 - t_2^2 \mp \sqrt{X_1}}{2(t_1 + \gamma)t_2},$$
$$\beta_{3(4)}(E) = \frac{E^2 + \gamma^2 - t_1^2 + 2Et_3 + t_3^2 - t_2^2 \mp \sqrt{X_2}}{2(t_1 + \gamma)t_2}, \tag{12}$$

where $X_{1(2)} = 4(\gamma^2 - t_1^2)t_2^2 + \{\gamma^2 - t_1^2 + t_2^2 + [E + (-)t_3]\}^2$. We can infer the size of the root under the parameters, i.e., $|\beta_1(E)| \leq |\beta_2(E)| \leq \cdots \leq |\beta_4(E)|$. The GBZ and E can be obtained by solving the equation $|\beta_i(E)| = |\beta_j(E)|$, where i, j are the middle two indexes.

In Figs. 2(a) and (b), we plot the spectra of $|\beta(E)| - t_1$. The green, blue, black and red lines represent the roots $|\beta_1(E)|$, $|\beta_2(E)|$, $|\beta_3(E)|$, and $|\beta_4(E)|$. We can know in Fig. 2(a) that when $\gamma = 0.5$, the roots meet at the points of $t_1 = \pm t_{TP1} = \pm 1.12$. In Fig. 2(b), it shows that when $\gamma = 1.5$, the roots can meet at the points of $t_1 = \pm t_{TP1} = \pm 1.80$, and the roots $|\beta_3(E)|$ and $|\beta_4(E)|$ is closed at $t_1 = \pm t_{TP2} = \pm 1.12$. At this case, all the roots satisfy $|\beta_1(E)| < |\beta_3(E)| = |\beta_4(E)| < |\beta_2(E)|$, which are consistent with the conclusion of GBZ. The above

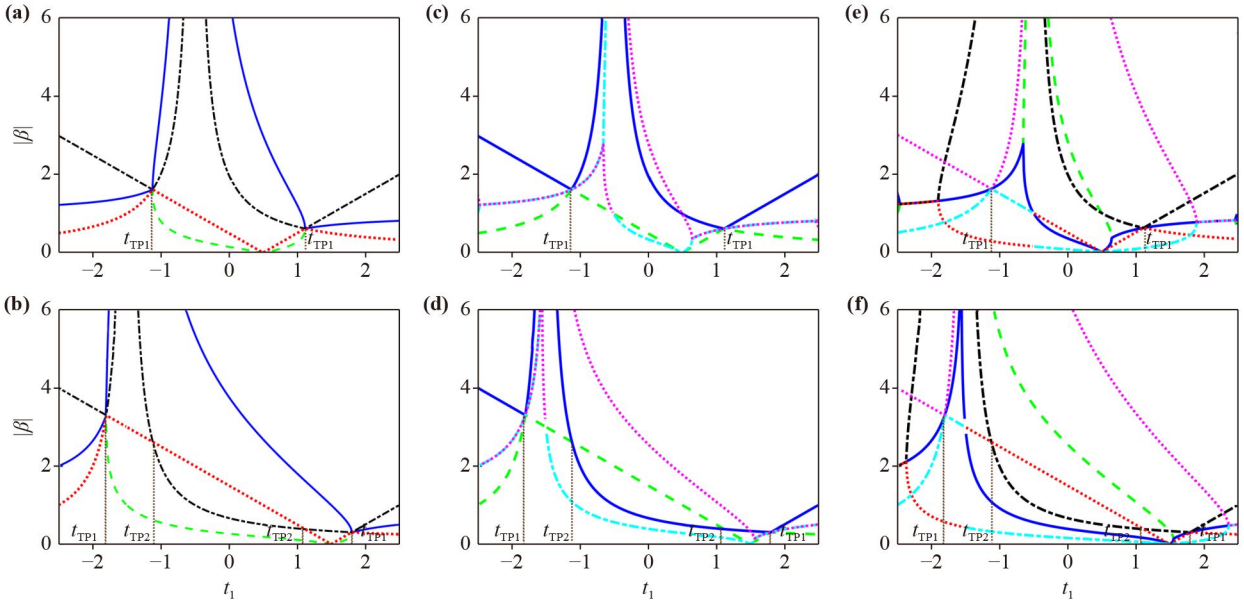

Fig. 2 Spectra of $|\beta(E)|$ with the change of t_1, under the condition of $t_2 = 1.0$ when $\gamma = 0.5$ **(a, c, e)** and $\gamma = 1.5$ **(b, d, f)**. To be specific, (a) and (b) describe the result of $E = \pm t_3$ for $M = 2$. (c) and (d) indicate the case of $E = 0$ when $M = 3$. (e) and (f) correspond to the case of $E = \sqrt{2}t_3$ at $M = 3$. Different color lines describe the different roots $|\beta(E)|$.

numerical results also obey the conclusion of the topological phase transition condition [i.e., Eq. (10)]. This exactly means that the system does undergo the topological phase transition at $t_1 = \pm\sqrt{t_2^2 + \gamma^2}$ and $t_1 = \pm\sqrt{\gamma^2 - t_2^2}$.

2.2 Cases of $M = 3$

We continue to pay attention to the case of $M = 3$, where the unit cell of the system becomes a six-sublattice structure ($a_{1,n}$, $b_{1,n}$, $a_{2,n}$, $b_{2,n}$, and $a_{3,n}$, $B_{b,n}$). Thus, the Hamiltonian can be written as $H = \sum_{n=1}^{N}[t_{1L}(a_{1,n}^{\dagger}b_{1,n} + a_{2,n}^{\dagger}b_{2,n} + a_{3,n}^{\dagger}b_{3,n}) + t_{1R}(b_{1,n}^{\dagger}a_{1,n} + b_{2,n}^{\dagger}a_{2,n} + b_{3,n}^{\dagger}a_{3,n})] + \sum_{n=1}^{N-1} t_2 \cdot (b_{1,n}^{\dagger}a_{1,n+1} + b_{2,n}^{\dagger}a_{2,n+1} + b_{3,n}^{\dagger}a_{3,n+1} h.c.) + \sum_{n=1}^{N} t_3(a_{1,n}^{\dagger}a_{2,n} + b_{1,n}^{\dagger}b_{2,n} + a_{2,n}^{\dagger}a_{3,n} + b_{2,n}^{\dagger}b_{3,n} + h.c.)$. The wavefunction of system is $|\Psi\rangle = (\psi_{a,1,1}, \cdots, \psi_{b,1,N}, \psi_{a,2,1}, \cdots, \psi_{b,2,N}, \psi_{a,3,1}, \cdots, \psi_{b,3,N})^{\mathrm{T}}$.

According to the discussion above, we first solve the topological phase transition condition by carrying out the similarity transformation $\bar{H} = S^{-1}HS$ and $|\bar{\Psi}\rangle = S^{-1}|\Psi\rangle$. In this similarity transformation, S is a diagonal matrix with the diagonal elements are $\{1, r, r, r^2, \cdots, r^{N-1}, r^N, 1, r, r, r^2, \cdots, r^{N-1}, r^N, 1, r, r, r^2, \cdots, r^{N-1}, r^N\}$, where $r = \sqrt{|t_{1R}/t_{1L}|}$. Although the increase of the lay number of this SSH structure, we know that the non-Hermitian Hamiltonian can also change to be Hermitian when the hopping terms satisfy $\tilde{t}_1 = \sqrt{|(t_1 - \gamma)(t_1 + \gamma)|}$, $\tilde{t}_2 = t_2$, and $\tilde{t}_3 = t_3$. Thus, in the momentum space, the Hamiltonian $\bar{H}$ after similarity transformation is given as

$$\bar{H}(k) = \begin{pmatrix} 0 & T_1 & t_3 & 0 & 0 & 0 \\ T_1^* & 0 & 0 & t_3 & 0 & 0 \\ t_3 & 0 & 0 & T_1 & t_3 & 0 \\ 0 & t_3 & T_1^* & 0 & 0 & t_3 \\ 0 & 0 & t_3 & 0 & 0 & T_1 \\ 0 & 0 & 0 & t_3 & T_1^* & 0 \end{pmatrix}, \tag{13}$$

where $T_1 = \tilde{t}_1 + t_2 e^{-ik}$. The energy expression for the Hermitian case can be expressed by diagonalizing the above Hamiltonian, i.e.,

$$\begin{aligned} \bar{E}_{1(2)} &= \pm\sqrt{Y_0}, \\ \bar{E}_{3(4)} &= \pm\sqrt{Y_1 - 2\sqrt{2Y_0}t_3}, \\ \bar{E}_{5(6)} &= \pm\sqrt{Y_1 + 2\sqrt{2Y_0}t_3}, \end{aligned} \tag{14}$$

with $Y_1 = t_2^2 + \tilde{t}_1^2 + 2t_3^2 + 2\tilde{t}_1 t_2 \cos k$. The topological phase transition occurs at $\tilde{t}_1 = t_2$, namely,

$$t_1 = \pm\sqrt{t_2^2 + \gamma^2}, \quad \text{or} \quad t_1 = \pm\sqrt{\gamma^2 - t_2^2}. \tag{15}$$

When the hopping parameters satisfy the relationships in the above equations, the six bands are in contact with each other at $k = \pi$. Namely, the bands of $\bar{E}_1$ and $\bar{E}_2$ meet at $\bar{E} = 0$, and those of $\bar{E}_{3(4)}$ and $\bar{E}_{5(6)}$ encounter at $\bar{E} = +(-)\sqrt{2}t_3$. Therefore, we can infer that in the case of $M = 3$, the system possesses two types of isolated modes.

Similar to the case of $M = 2$, we can also solve for the roots $|\beta(E)|$. By replacing $e^{ik}(e^{-ik})$ with $\beta(\beta^{-1})$, $H(\beta)$ can be re-expressed as

$$H(\beta)=\begin{pmatrix} 0 & B_1 & t_3 & 0 & 0 & 0 \\ B_2 & 0 & 0 & t_3 & 0 & 0 \\ t_3 & 0 & 0 & B_1 & t_3 & 0 \\ 0 & t_3 & B_2 & 0 & 0 & t_3 \\ 0 & 0 & t_3 & 0 & 0 & B_1 \\ 0 & 0 & 0 & t_3 & B_2 & 0 \end{pmatrix}, \tag{16}$$

in which $B_1=(t_1+\gamma)+t_2\beta^{-1}$ and $B_2=(t_1-\gamma)+t_2\beta$. The solutions of the eigenvalue equation $|H(\beta)-E|=0$ can be written explicitly, i.e., $E_{1(2)}(\beta)=\pm\sqrt{[\beta(\gamma+t_1)+t_2](-\gamma+t_1+\beta t_2)/\beta}$, $E_{3(4)}(\beta)=\pm\{[\beta(-\gamma+t_1)t_2+\beta^3(\gamma+t_1)t_2+\beta^2(-\gamma^2+t_1^2+2t_3^2+t_2^2)-Z]/\beta\}^{\frac{1}{2}}$, and $E_{5(6)}(\beta)=\pm\{[\beta(-\gamma+t_1)t_2+\beta^3(\gamma+t_1)t_2+\beta^2(-\gamma^2+t_1^2+2t_3^2+t_2^2)+Z]/\beta\}^{\frac{1}{2}}$, where $Z=-2\sqrt{2}\{\beta^3t_3^2[\beta(\gamma+t_1)+t_2](-\gamma+t_1+\beta t_2)\}^{\frac{1}{2}}$. And then, we can obtain the complex roots of $E(\beta)$, namely,

$$\begin{aligned}
\beta_{1(2)}(E)&=\frac{1}{2t_2(\gamma+t_1)}[E^2-\gamma^2-t_1^2-t_2^2\mp\sqrt{4(\gamma^2-t_1^2)t_2^2+(E^2+\gamma^2-t_1^2-t_2^2)^2}],\\
\beta_{3(4)}(E)&=\frac{1}{2(\gamma+t_1)t_2}[E^2+\gamma^2-t_1^2-t_2^2+2t_3^2-2\sqrt{2E^2t_3^2}\mp(\gamma+t_1)\sqrt{Z_1}],\\
\beta_{5(6)}(E)&=\frac{1}{2(\gamma+t_1)t_2}[E^2+\gamma^2-t_1^2-t_2^2+2t_3^2+2\sqrt{2E^2t_3^2}\mp(\gamma+t_1)\sqrt{Z_2}],
\end{aligned} \tag{17}$$

where

$$Z_1=\Delta_0-\Delta_1+\frac{2t_2^2+4\sqrt{2}t_2^2|Et_3/(\gamma+t_1)|-\Delta_2-\Delta_3}{\gamma+t_1},$$
$$Z_2=\Delta_0+\Delta_1+\frac{2t_2^2-4\sqrt{2}t_2^2|Et_3/(\gamma+t_1)|+\Delta_2-\Delta_3}{\gamma+t_1}.$$

$\Delta_0=2E^2+(\gamma-t_1)^2+4t_3^2$, $\Delta_1=4\sqrt{2}|\frac{Et_3}{(\gamma+t_1)t_2}|(\gamma-t_1t_2)$, $\Delta_2=4\sqrt{2}|\frac{Et_3}{(\gamma+t_1)t_2}|(E^2-2t_3^2)$, and $\Delta_3=4t_1(E^2+t_2^2+2t_3^2)-\frac{E^4+2E^2(6t_3^2-t_2^2)+(t_2^2-2t_3^2)^2}{\gamma+t_1}$. Figures 2(c)–(f) show the curves of $|\beta(E)|-t_1$ in the case of $\gamma=0.5$ and 1.5, respectively. The blue, green, black, red, light-blue and pink lines represent the roots from $|\beta_1(E)|$ to $|\beta_6(E)|$, respectively. In Figs. 2(c) and (d), we present the results of $E=0$. It can be found that the curves of $|\beta_{3(5)}(E)|$ and $|\beta_{4(6)}(E)|$ are the same as each other. For $\gamma=0.5$, the curves of $|\beta_{1,2,5,6}(E)|$ meet at $t_1=\pm t_{TP1}=\pm1.12$ [see Fig. 2(c)]. Alternatively, in Fig. 2(d) it shows that when $\gamma=1.5$, the roots are closed at $t_1=\pm t_{TP1}=\pm1.8$, and the curves of two roots $|\beta_1(E)|$ and $|\beta_2(E)|$ ($|\beta_5(E)|<|\beta_1(E)|=|\beta_2(E)|<|\beta_6(E)|$) meet at $t_2=\pm t_{TP2}=\pm1.12$. The results for t_{TP1} and t_{TP2} are consistent with the conclusion of Eq. (15). Similar to $E=0$, it can be clearly observed from Figs. 2(e) and (f) that the curves of $|\beta_5(E)|$ and $|\beta_6(E)|$ meet at $\pm t_{TP1}$ when $\gamma=0.5$ or 1.5. In addition, when $\gamma=1.5$, the roots $|\beta_3(E)|$ and $|\beta_4(E)|$ ($|\beta_5(E)|<|\beta_1(E)|<|\beta_3(E)|=|\beta_4(E)|<|\beta_2(E)|<|\beta_6(E)|$) are closed at $\pm t_{TP2}$. The results of t_{TP1} and t_{TP2} are also same as those in Eq. (15). Based on the above results, the system undergoes topological phase transition under $t_1=\pm\sqrt{t_2^2+\gamma^2}$ and $t_1=\pm\sqrt{\gamma^2-t_2^2}$.

From the results of $M=2$ and $M=3$ above, we can further determine that the topological phase transition conditions can be accurately derived by performing the similarity transformation in our consider the multilayer SSH structure. Therefore, we would like to utilize the similar methods to calculate the topological phase transition for the case of larger M. Accordingly, the non-Hermitian system can be described by a new Hermitian Hamiltonian $\bar{H}=S^{-1}HS$, with the wavefunction defined as $|\bar{\Psi}\rangle=S^{-1}|\Psi\rangle$. After calculation, the new hopping terms of the Hermitian Hamiltonian are given as $\tilde{t}_1=\sqrt{|(t_1+\gamma)(t_1-\gamma)|}$, $\tilde{t}_2=t_2$ and $\tilde{t}_3=t_3$. When the band gaps are closed at $k=\pi$, the system will undergo the topological phase transition, with the topological phase transition conditions being $t_1=\pm\sqrt{t_2^2+\gamma^2}$ or $t_1=\pm\sqrt{\gamma^2-t_2^2}$.

3 Numerical results and discussion

In this section, we proceed to numerically discuss the band structure of the multilayer nonreciprocal SSH structure in detail, under the open boundary condition. Before discussion, we would like to state the order of discussion under the open boundary condition as follows. Firstly, we plot the energy spectra and observe the characteristics of the band structure. Secondly, we introduce inverse participation rate (IPR) to characterize the local properties of the system. Next, from the energy and probability density spectra, the localization of various edge modes is discussed. Finally, the robustness of edge modes to disorder under different structures is observed by two off-diagonal disorders. In addition, we take $t_2=1.0$ in the context to perform the calculation for convenience.

3.1 Cases of $M=1$ and $M=2$ under OBC

Before our discussion, we would like to review the case of $M=1$. When $M=1$, the system reduces to a one-dimensional nonreciprocal SSH structure. According to the previous works [49, 70], in the presence of nonreciprocal couplings, the system undergoes gap closing and reopening as the strength of the hopping coefficient changes. This theoretical results show that the system undergoes the topological phase transition at $t_1=\sqrt{t_2^2+\gamma^2}$ and $t_1=-\sqrt{t_2^2+\gamma^2}$, respectively. The twofold-degenerate

zero-energy modes appear between these two transition points. From the spectrum of energy imaginary part, one can find that the energy spectrum is real in other regions where the energy imaginary part emerges in the range of $|t_1| < |\gamma|$. Moreover, the twofold-degenerate zero-energy modes do always not display their imaginary part. More importantly, with the increase of γ, the zero-energy modes undergo splitting. As shown by the local density of states spectra in Refs. [49, 70], the wavefunctions show a tendency to be localized at one boundary of the system for both bulk and zero-energy modes. All these results should be attributed to the non-Hermitian skin effect.

Following the result of $M = 1$, we continue to discuss the band structure in the case of $M = 2$. Figures 3(a)–(d) show the real and imaginary parts of energy bands under the condition of $t_2 = t_3 = 1.0$. From the spectra of the real and imaginary parts of energy, one can find that γ takes different effects on the bulk states and isolated modes of this system. In Figs. 3(a) and (b) where $\gamma = 0.5$, the energy gap is closed at the points $t_1 = -1.12$ and $t_1 = 1.12$, respectively. Between these two critical points, isolated modes appear in the band gap. In addition, we notice that the isolated modes at this point are no longer zero-energy modes but the isolated modes with eigenvalues of $E = \pm 1.0$. This phenomenon is different from the result in the one-dimensional SSH chain of $M = 1$. Next, the spectrum of the imaginary part of energy shows that it appears in the range of $t_1 \in [-0.5, 0.5]$. This indicates that the nonreciprocal coupling induces the appearance of complex eigenvalues of bulk states. However, the imaginary part of isolated modes is always equal to zero in such a case. With the increase of nonreciprocal coupling strength γ, the range of isolated modes becomes wider. When γ is increased to a critical value, the isolated modes split, and their range becomes narrower. For example, in the case of $\gamma = 1.5$, isolated modes of $E = \pm 1.0$ only exist in the range of $t_1 \in [-1.8, -1.12] \cup [1.12, 1.8]$. In the range of $-1.12 < t_1 < 1.12$, they split into two modes. Such numerical results of critical points and energies are consistent with the derivations results $t_1 = \pm\sqrt{t_2^2 + \gamma^2}$ and $E = \pm t_3$ in Section (2.1). For the bulk-states, the increase of γ drives a gradual expansion of the imaginary-energy range. Now, we can make a conclusion that this system is allowed to display the nonzero energy modes in the band gap, under the condition of $M = 2$. The nonreciprocal coupling parameter γ plays its significant modulation role in the appearance of isolated modes and bulk states.

To further understand the band-structure characteristics of this system before and after the similarity transformation, i.e., the non-Hermitian H and Hermitian $\bar{H}$, in Figs. 3(e) and (f) we present the spectra of $|E|$ of an open chain as a function of t_1 in the cases of $\gamma = 0.5$ and $\gamma = 1.5$, respectively. The blue lines describe the model of the non-Hermitian multilayer nonreciprocal SSH

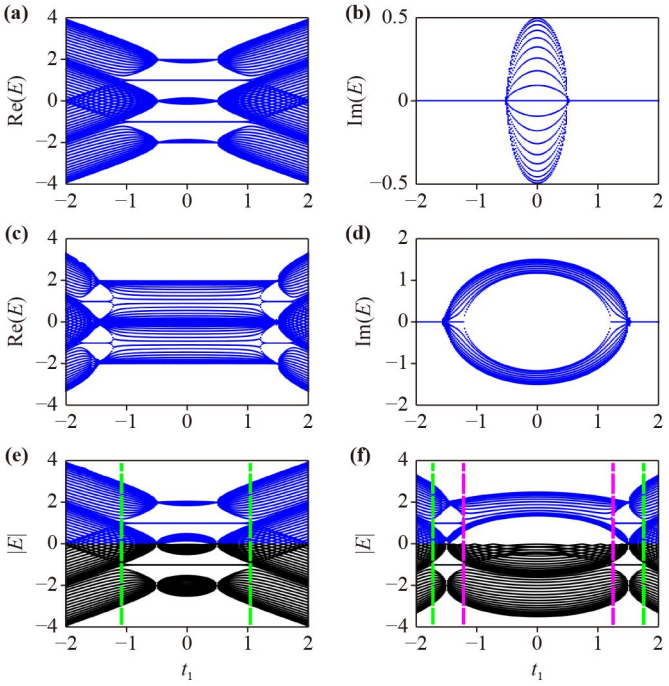

Fig. 3 **(a–d)** OBC energy spectra with the change of t_1, where (a, b) $\gamma = 0.5$, and (c, d) $\gamma = 1.5$. The left column is the real part of eigenenergies, and the right column is the corresponding imaginary part. **(e, f)** Spectra of $|E|$ as a function of t_1 when $\gamma = 0.5$ and $\gamma = 1.5$, respectively. Blue lines are related to the non-Hermitian multilayer nonreciprocal SSH structure, and black lines correspond to the Hermitian system after similarity transformation. Parameters are taken to be $t_2 = t_3 = 1.0$.

structure, whereas the black lines represent the corresponding Hermitian result after similarity transformation. We clearly observe that for the bulk states, there are some differences between the eigenvalues of H and $\bar{H}$. However, for isolated modes, the open-boundary energy spectra of H and $\bar{H}$ are the same regardless of $\gamma = 0.5$ or $\gamma = 1.5$. Thus, identical topological critical points appear in the energy spectra, namely, such two Hamiltonians enable to exhibit the same topological phase transition. Meanwhile, the energies of isolated modes in both cases are the same as each other. This exactly suggests that it is valid to discuss the non-Hermitian Hamiltonian with the help of the results after similarity transformations in the structure of $M = 2$, and the non-Hermitian topological properties can be judged from the Hermitian Hamiltonian $\bar{H}$ after similarity transformation.

In Fig. 4, we provide the eigenenergy spectra and wavefunction probability density distribution. Besides, in order to characterize the various types of states, we introduce the inverse participation rate (IPR) to describe the localization of the wavefunction in more detail. According to the previous works [71–75], the expression of IPR is defined as

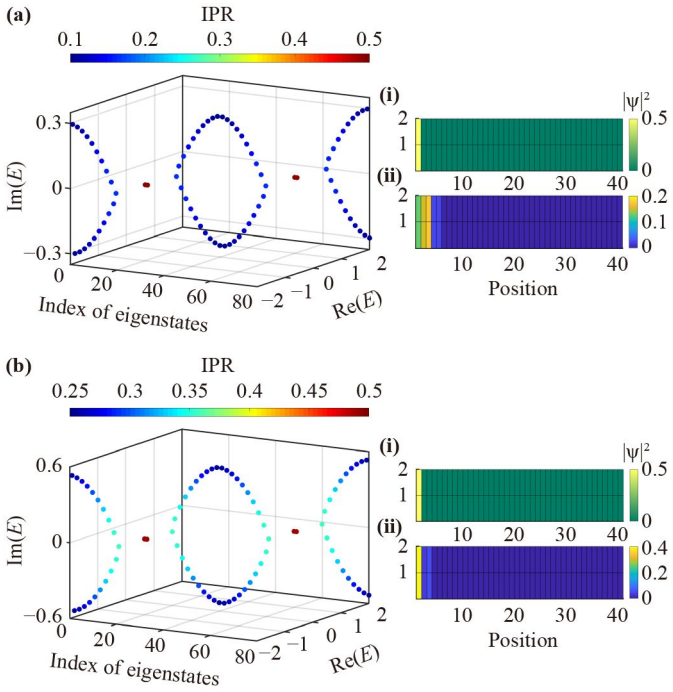

Fig. 4 Eigenenergy spectra and wavefunction probability density distribution under OBC. The colors represent the values of IPR, where **(a)** $\gamma = 0.5$ and $t_1 = 0.4$, **(b)** $\gamma = 1.5$ and $t_1 = 1.4$. The right column corresponds to the wavefunction probability density distribution of edge modes and bulk states. Other parameters are set to be $t_2 = t_3 = 1.0$.

$$\mathrm{IPR}_n = \frac{\sum_l |\psi_n(l)|^4}{(\sum_l |\psi_n(l)|^2)^2}, \tag{18}$$

where ψ_n is the n-th right eigenvector of H [69, 71–73], and l is the site index of the considered system. Usually, IPR is used to calculate the localization degree of each state and quantitatively describe the wavefunction localization. IPR_n of the localized states tends to be a nonzero and finite value with the increase of the system's size L. It has been found that $\mathrm{IPR}_n \to 1.0$ for the completely-localized states [71–73].

Figure 4(a) describes the case of $\gamma = 0.5$ with $t_1 = 0.4$. The colors represent the values of IPR. We can find that the system has four bands due to the presence of four sublattices. For the bulk bands, the imaginary part of energy is mainly contributed by the bulk states. Moreover, the isolated modes are twofold degenerate and the imaginary part of energy $\mathrm{Im}(E) = 0$. By observing the value of IPR, it can be seen that IPR of isolated modes are equal to $\mathrm{IPR}_{20,21} = \mathrm{IPR}_{60,61} = 0.49$, and the IPR value of the bulk states is about $\mathrm{IPR} \sim 0.1$. These results indicate that the bulk states are less localized than isolated modes. The right column figures (i) and (ii) show the spectra of wavefunction probability density distribution about isolated modes and bulk states, respectively. One can clearly find that the system displays the non-Hermitian skin effect. To be specific, the result in (i) corresponds to the probability density spectra of $E = \pm t_3 = \pm 1.0$. We can find that the isolated modes are the edge modes. They are only localized in sublattices $a_{1,1}$ and $a_{2,1}$ and wavefunction satisfies $|\psi_{a,1,1}|^2 = |\psi_{a,2,1}|^2$. The figure (ii) shows the probability density spectra of $E = -1.97 - 0.18\mathrm{i}$ of bulk band. It shows that it has the tendency to be localized on the left side.

In Fig. 4(b), we present the spectra in the case of $\gamma = 1.5$ with $t_1 = 1.4$. The right column figures (i) and (ii) represent the wavefunction probability density distribution of isolated modes and bulk states, respectively. For the isolated modes, the results are the same as those of $\gamma = 0.5$. The twofold degenerate edge modes are also localized at $a_{1,1}$ and $a_{2,1}$ and the IPR also satisfies $\mathrm{IPR} = 0.49$. However, for the IPR of bulk bands, we find that the IPR increases in the range of $0.2 < \mathrm{IPR} < 0.35$. This phenomenon means the further localization of bulk states as γ increases. The wavefunction probability density can also verify this result. It can be seen that the wavefunction tends to be localized on the left side of the system and more localized in comparison with those in the case of $\gamma = 0.5$. Up to now, we have known that there exist twofold degenerate edge modes localized on one side of the system boundary in the system of $M = 2$. Also, increasing γ does not change the energy of edge modes, and the energy still satisfies $E = \pm t_3$ in the energy gap.

We can also explain these phenomena by solving the Schrödinger equation of this structure [29]. From $H\Psi = E\Psi$, we can write out the Schrödinger equations of the edge modes:

$$\begin{aligned}
&(t_1 + \gamma)\psi_{b,1(2),1} + t_3\psi_{a,2(1),1} = E\psi_{a,1(2),1}, \\
&(t_1 - \gamma)\psi_{a,1(2),1} + t_3\psi_{b,2(1),1} + t_2\psi_{a,1(2),2} = E\psi_{b,1(2),1},
\end{aligned} \tag{19}$$

where $\psi_{\alpha,m,n}$ is the wavefunction of sublattice α in the mth layer of the nth unit cell. According to the wavefunction distribution in Fig. 4, the edge modes are only contributed by $\psi_{a,1,1}$ and $\psi_{a,2,1}$. The edge modes localized on the left side satisfy $\psi_{b,1,1} = \psi_{b,2,1} = 0$, so the edge-mode eigenvalues can be ascertained, i.e., $E^2 - t_3^2 = 0$. The expressions of energy and wavefunction can be written as $E = \pm t_3$ and $\psi_{a,1,1} = \frac{t_3}{E}\psi_{a,2,1}$, respectively. For $E = t_3$, the wavefunction amplitude yields $\frac{|\psi_{a,1,1}|^2}{|\psi_{a,2,1}|^2} = 1$. Therefore, the localization characteristic is the same as the localization strength at $|\psi_{a,1,1}|$ and $|\psi_{a,2,1}|$ when the energy is aligned with the edge-mode energy. These results correspond to those in Figs. 3 and 4.

3.2 Case of $M = 3$ under OBC

In this part, we focus on the case of triple-layer SSH structure with $M = 3$, where the three chains are coupled

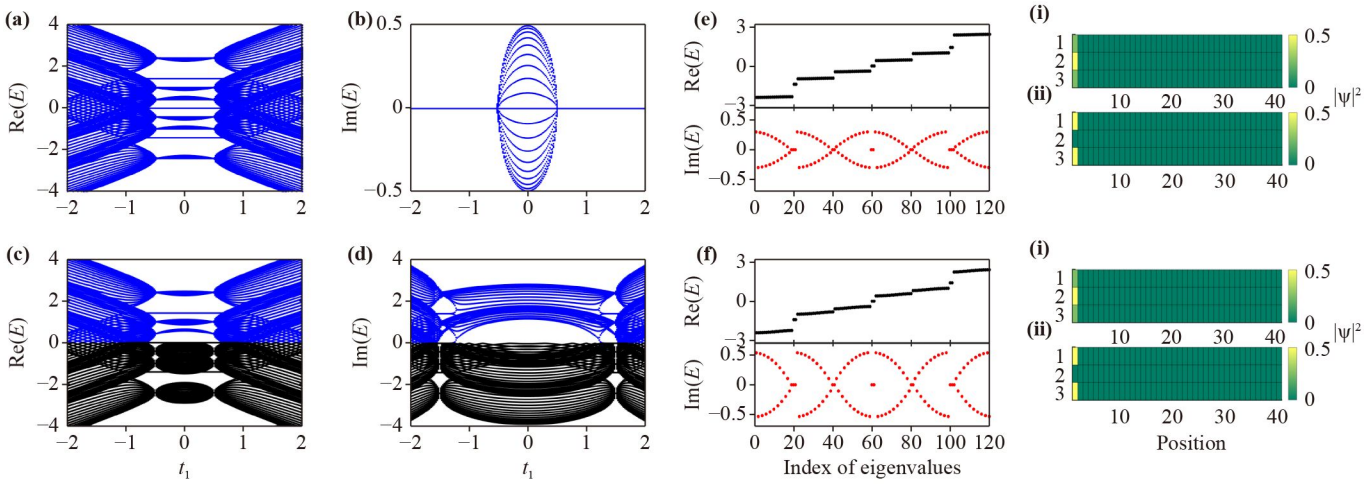

Fig. 5 **(a, b)** OBC energy spectra with the change of t_1, where $\gamma = 0.5$. The left column is the real part of the eigenenergies, and the right column is the corresponding imaginary part. **(c, d)** Spectra of $|E|$ as a function of t_1 when $\gamma = 0.5$ and $\gamma = 1.5$, respectively. Blue lines for the non-Hermitian multilayer nonreciprocal SSH structure, and black lines denote the corresponding Hermitian system after similarity transformation. **(e, f)** Eigenenergy and probability density spectra. The right column represents the localization probability density of edge modes. Relevant parameters are set as (a) $t_1 = 0.4$ and $\gamma = 0.5$, and (b) $t_1 = 1.4$ and $\gamma = 1.5$. The others are taken to be $t_2 = t_3 = 1.0$.

together to form a six-sublattice configuration. To perform calculation, we also set $t_2 = t_3 = 1.0$. Similar to the case of $M = 2$, the structural characteristics of this system are still discussed from the energy-band spectra, as shown in Figs. 5(a)–(d). To be specific, Figs. 5(a) and (b) show the real and imaginary parts of energy where $\gamma = 0.5$. In this figure we can find that this system has six energy bands which are determined by the number of sublattice. Regarding the isolated modes, we can clearly observe that this system have two kinds of isolated modes with different energies, i.e., the first is $E = \pm 1.41 = \sqrt{2}t_3$, the other is $E = 0$. The two kinds of isolated modes exist around two critical points $t_1 = \pm 1.12 = \pm\sqrt{t_2^2 + \gamma^2}$. These numerical results are consistent with the theoretical derivation. Besides, the eigenenergies of these two isolated modes are also real. On the other hand, Figs. 5(c) and (d) present the spectra of energy absolute value $|E|$ of non-Hermitian Hamiltonian H (blue lines) and Hermitian Hamiltonian $\bar{H}$ (black lines) before and after similarity transformations. It can be found that two situations have the obvious difference in the bulk states. However, for the isolated modes, both the energy value and the appearance range are consistent. This also indirectly proves that the similarity transformations are effective to discuss the topological phase transition.

To observe the localization effect of the two isolated modes as well as the bulk states, in Figs. 5(e) and (f) we plot the eigenenergy and the probability density spectra. In the case of $\gamma = 0.5$ with $t_1 = 0.4$ [see Fig. 5(e)], it can be seen that three pairs of twofold degenerate isolated modes arise in the band gap, with their purely-real energies. In the right column, (i) and (ii) show the probability density spectra of the two different modes $E = \pm t_3 = \pm 1.41$ and $E = 0$, respectively. We find that although both of the modes exhibit localization on the left side of the system, their localization effects are different from each other. In more detail, for the first edge modes $E = \pm 1.41$ (i), the wavefunction is localized to the far left of the system ($a_{1,1}$, $a_{2,1}$ and $a_{3,1}$), and in the other region the wavefunctions are almost equal to zero. In the case of $E = 0$ (ii), the modes are only localized at sublattices $a_{1,1}$ and $a_{3,1}$, showing strong localization. This result can also be observed in the case of $\gamma = 1.5$. For $\gamma = 1.5$ with $t_1 = 1.4$, the edge modes also belong to twofold degenerate states and the eigenenergy cannot be changed with the increment of γ [see Fig. 5(f)]. For the probability density spectra, (i) and (ii) correspond to $E = \pm 1.414$ and $E = 0$, respectively. The localization does not change in these edge modes, and the edge modes are the same as the those of $\gamma = 0.5$.

Next, we introduce IPR to characterize the localization characteristics of the system. Figure 6 shows the results of IPR of bulk bands and edge modes. The magnitudes of IPR describe numerically the localization properties of the respective states. To be specific, we find that the values of IPR are manifested as $\text{IPR} \sim (0.08 - 0.16)$ for the bulk bands. For example, the range of IPR for first (third)-class bulk bands $E \in [\pm 2.41(1.00) \pm 0.30\text{i} \sim \pm 2.36(0.95)]$ is $0.08 < \text{IPR} < 0.12$, and the value of IPR for second-class bulk bands $E \in (\pm 1.00 \pm 0.30\text{i} \sim \pm 0.95)$ is $0.10 < \text{IPR} < 0.16$. According to the numerical results of IPR, we can infer that the second-class bulk bands have slightly better locality than the others, whereas the first and third class bulk bands could have similar localization properties. For two kinds of edge modes, one is equal to

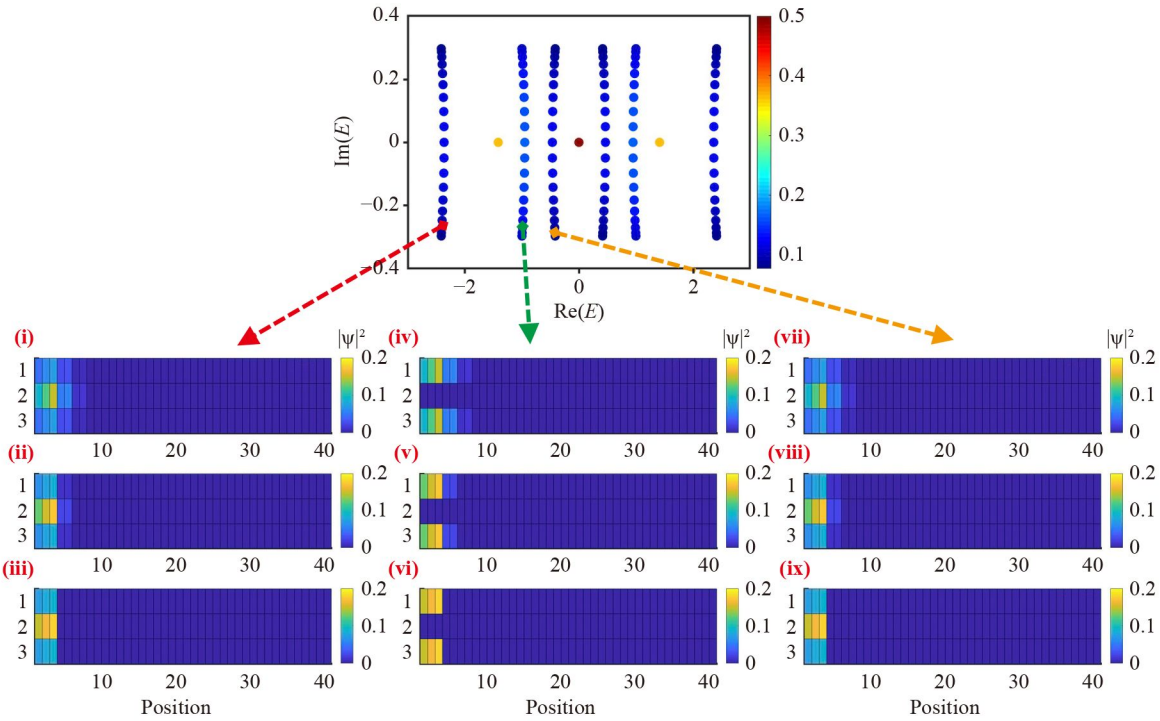

Fig. 6 Eigenenergy spectra in $M = 3$, for the case of $\gamma = 0.5$. The colors represent the values of IPR. (i–ix) Probability density spectra of these three-classes bulk bands. (i–iii) represent the localization probability density of $E = \pm 2.41 \pm 0.30\mathrm{i}$, $E = \pm 2.38 \pm 0.18\mathrm{i}$, and $E = \pm 2.36$, respectively; (iv–vi) shows the probability density in the cases of $E = \pm 1.0 \pm 0.30\mathrm{i}$, $E = \pm 0.97 \pm 0.18\mathrm{i}$, and $E = \pm 0.95$, respectively; (vii–ix) stand for the probability density of $E = \pm 0.42 \pm 0.30\mathrm{i}$, $E = \pm 0.45 \pm 0.18\mathrm{i}$, and $E = \pm 0.47$, respectively. Relevant parameters are taken to be $t_1 = 0.4$, $t_2 = t_3 = 1.0$.

IPR $= 0.37$ when $E = \pm\sqrt{2}t_3$ and the other is IPR $= 0.49$ when $E = 0$. It means that the edge modes of $E = 0$ are more localized than modes of $E = \pm\sqrt{2}t_3$, and these results agree with those in Figs. 5(e) and (f).

In order to identify the localization effect of the bulk states, Figs. 6(i)–(ix) show the localization of the bulk states in different energy bands. It can be observed that both the bulk states and edge modes have the tendency to be on one side of the system, so the whole system has the non-Hermitian skin effect. However, each energy band has the respective localization effects.

For the first-class bulk band (red arrow line), the spectra of (i)–(iii) represent localization probability density $E = \pm 2.41 \pm 0.30\mathrm{i}$, $E = \pm 2.38 \pm 0.18\mathrm{i}$ and $E = \pm 2.36$, respectively. We see that the the first-class bulk states are more localized on the second chain $(a_{2,n}, b_{2,n})$, although all three chains have local effects. For the second-class bulk bands (green arrow line), probability density spectra of (iv)–(vi) correspond to $E = \pm 1.00 \pm 0.30\mathrm{i}$, $E = \pm 0.97 \pm 0.18\mathrm{i}$, and $E = \pm 0.95$, respectively. Unlike the first-class bulk bands, the second-class bulk bands are only localized in the first chain $(a_{1,n}, b_{1,n})$ and the third chain $(a_{3,n}, b_{3,n})$, whereas the second chain shows a trend of empty occupation. In the third-class bulk bands (yellow arrow line), the (vii)–(ix) show the probability density spectra of $E = \pm 0.42 \pm 0.30\mathrm{i}$, $E = \pm 0.45 \pm 0.18\mathrm{i}$ and $E = \pm 0.47$, respectively. It can be found that the localization properties are the same as the first-class bulk band. The comparison of the three energy bands reveals that the localization effect of the second-class bulk bands is indeed slightly better than the other two bulk bands. In addition, all three bulk bands have similar localization effects, that is, the localization of the bulk states becomes better as the energy imaginary part gradually decreases. These results are completely the same as the numerical results of IPR in Fig. 6(a).

Following all the above discussions, we understand that when three non-Hermitian SSH chains are coupled to one another, two different topological edge modes appear in the band gap, i.e., the first is the twofold degenerate edge modes with energy $E = \pm\sqrt{2}t_3$ and the second is the double degenerate zero-energy modes. The bulk states show different local effects with the number of the bulk bands, which exhibits special parity effect. Compared with the case of $M = 2$, the whole system displays a richer variety of topological edge modes. The causes of the generation of the properties of the two edge modes and bulk bands can also be explained in the form of Schrödinger equation. According to $H\Psi = E\Psi$,

the Schrödinger equation for the two edge modes satisfies:

$$\begin{aligned}
&(t_1+\gamma)\psi_{b,1(3),1}+t_3\psi_{a,2,1}=E\psi_{a,1(3),1},\\
&(t_1-\gamma)\psi_{a,1(3),1}+t_3\psi_{b,2,1}+t_2\psi_{a,1(3),2}=E\psi_{b,1(3),1},\\
&t_3\psi_{a,1,1}+(t_1+\gamma)\psi_{b,2,1}+t_3\psi_{a,3,1}=E\psi_{a,2,1},\\
&t_3\psi_{b,1,1}+(t_1-\gamma)\psi_{a,2,1}+t_3\psi_{b,3,1}+t_2\psi_{a,2,2}=E\psi_{b,2,1},
\end{aligned} \tag{20}$$

For the edge modes with energy $E=0$, according to the wavefunction probability density in Fig. 5(e), we can set $\psi_{b,1,1}=\psi_{a,2,1}=\psi_{b,2,1}=\psi_{b,3,1}=0$. Thus, the Schrödinger equation satisfies: $t_3\psi_{a,1,1}+t_3\psi_{a,3,1}=0$ and $\frac{|\psi_{a,1,1}|^2}{|\psi_{a,3,1}|^2}=1$. For the edge modes with energy $E=\pm\sqrt{2}t_3$, we can set $\psi_{b,1,1}=\psi_{b,2,1}=\psi_{b,3,1}=0$. Thus, the Schrödinger equation satisfies: $t_3\psi_{a,2,1}=E\psi_{a,1,1}$, $t_3\psi_{a,1,1}+t_3\psi_{a,3,1}=E\psi_{a,2,1}$ and $t_3\psi_{a,2,1}=E\psi_{a,3,1}$, we can obtain $E^2-t_3^2=0$. The expressions of energy and wavefunction can be written as: $E=\pm\sqrt{2}t_3$, $\psi_{a,1,1}=\frac{t_3}{E}\psi_{a,2,1}$ and $\psi_{a,3,1}=\frac{t_3}{E}\psi_{a,2,1}$. For $E=\sqrt{2}t_3$, the wavefunction amplitude yields $\frac{|\psi_{a,1,1}|^2}{|\psi_{a,2,1}|^2}=\frac{1}{2}$ and $\frac{|\psi_{a,1,1}|^2}{|\psi_{a,3,1}|^2}=1$.

We can also use the same method to verify some special positions of the bulk states. For example, when energy is equal to $E=\pm0.95$, according to the probability density spectra Fig. 6(vi), the Schrödinger equation can be simplified as $(t_1+\gamma)\psi_{b,1(3),1}=E\psi_{a,1(3),1}$, $(t_1-\gamma)\cdot\psi_{a,1(3),1}+t_2\psi_{a,1(3),2}=E\psi_{b,1(3),1}$, $t_3\psi_{a(b),1,1}+t_3\psi_{a(b),3,1}=0$, $t_2\psi_{b,1(3),1}=E\psi_{a,1(3),2}$ and $t_3\psi_{a,1,2}+t_3\psi_{a,3,2}=0$. We can get the expression $E^2-t_2^2-(t_1+\gamma)(t_1-\gamma)=0$, thus $E=\pm\sqrt{t_2^2+t_1^2-\gamma^2}$. The relationship of wavefunction amplitude can be written as $\frac{|\psi_{a,1,1}|^2}{|\psi_{a,3,1}|^2}=\frac{|\psi_{b,1,1}|^2}{|\psi_{b,3,1}|^2}=\frac{|\psi_{a,1,2}|^2}{|\psi_{a,3,2}|^2}=1$, $\frac{|\psi_{b,3,1}|^2}{|\psi_{a,3,1}|^2}=\frac{t_2^2+t_1^2-\gamma^2}{(t_1+\gamma)^2}$, $\frac{|\psi_{a,1,2}|^2}{|\psi_{b,1,1}|^2}=\frac{t_2^2}{t_2^2+t_1^2-\gamma^2}$ and $\frac{|\psi_{a,1,1}|^2}{|\psi_{b,1,1}|^2}=\frac{(t_1+\gamma)^2}{t_2^2+t_1^2-\gamma^2}$. When $\gamma=0.5$, $t_1=0.4$ and $t_2=t_3=1$, with the help of the above results, we can get $|\psi_{a,1,1}|=|\psi_{a,3,1}|=0.15$, $|\psi_{b,1,1}|=|\psi_{b,3,1}|=0.17$ and $|\psi_{a,1,2}|=|\psi_{a,3,2}|=0.18$. These results can match Fig. 6(vi) in an effective way.

According to the results from $M=1$ to $M=3$, We find that the three configurations have the same properties which can be presented as follows: (1) Nonreciprocal coupling γ causes the system to have imaginary parts of energy, which are derived from the bulk states, but the energies of edge modes are real. Besides, the system undergo the non-Hermitian skin effect. (2) The increase of γ does not modify the eigenenergy and localization of edge modes, but makes the localization of the bulk states stronger. (3) The larger γ, such as $\gamma=1.5$, causes the twofold degenerate edge modes to undergo splitting and transform into the nonzero energy modes. Of course, the three configurations also have respective unique properties. They can be summarized as: (I) For $M=1$ and $M=3$, the system has a purely-real twofold degenerate zero energy modes, but not for the case of $M=2$. We conjecture that there exists the "parity effect" in the system. (II) There is a numerical relationship between the energy of the edge modes and their corresponding eigenvalues. (I, II) For the case of $M=3$, three classes of bulk bands have different localizations, i.e., the first and the third class of bulk bands are similar, but they are completely different from the second type. We conjecture that another "parity effect" may also exist for different numbers of bulk states.

3.3 Cases of $M=4$ and $M=5$ under OBC

In the following, in order to better verify the conjectures (I)–(III) of these specific properties, we discuss in detail the cases $M=4$ and $M=5$. Based on the results above, we know that the case of high γ (e.g., $\gamma=1.5$) does not affect the energy bands and localization of the topological states. Therefore, the following mainly focuses on the case at $\gamma=0.5$.

Firstly, we would like to pay attention to the edge modes. Figure 7 shows the band structures of $M=4$ and $M=5$. When $M=4$, in Figs. 7(a)–(c) it is shown that the system contributes two kinds of edge modes with different eigenenergies, i.e., $E=\pm2.43=\pm\frac{1+\sqrt{5}}{2}t_3$ and $E=\pm0.93=\pm\frac{1-\sqrt{5}}{2}t_3$, which are existed between the positions of $t_1=\pm\sqrt{t_1^2+\gamma^2}=\pm1.12$. Besides, these two edge modes are twofold degenerate, as shown by the eigenenergy spectra. According to the probability density spectra of (i) and (ii), we can observe that although the two types of edge modes are both localized at the left side, these possess different localized properties. To be specific, the edge modes of $E=\pm2.43$ in (i) are mainly localized at the middle chains, i.e., sublattices $a_{2,1}$ and $a_{3,1}$, followed by $a_{1,1}$ and $a_{4,1}$. The wavefunction satisfies the relationship $\frac{|\psi_{a,1,1}|^2}{|\psi_{a,2,1}|^2}=\frac{|\psi_{a,4,1}|^2}{|\psi_{a,3,1}|^2}=\frac{2}{3+\sqrt{5}}$ and $\frac{|\psi_{a,2,1}|^2}{|\psi_{a,3,1}|^2}=1$. Alternatively, the localization of the edge modes with energy $E=\pm0.93$ in (ii) shows the opposite trend, and also, the wavefunction has the different relationships, i.e., $\frac{|\psi_{a,1,1}|^2}{|\psi_{a,2,1}|^2}=\frac{|\psi_{a,4,1}|^2}{|\psi_{a,3,1}|^2}=\frac{2}{3-\sqrt{5}}$ and $\frac{|\psi_{a,2,1}|^2}{|\psi_{a,3,1}|^2}=1$. Therefore, we can conclude that for the case formed by the coupling of four nonreciprocal chains, the whole system shows up as twofold degenerate edge modes with energies $E=\pm\frac{1+\sqrt{5}}{2}t_3$ and $E=\pm\frac{1-\sqrt{5}}{2}t_3$.

Figure 7(d)–(f) show the energy and probability density spectra under the case of $M=5$ with $t_3=2.0$. It is observed that the system has three pairs of twofold degenerate edge modes in the band gaps, with their different energies. Namely, the first is $E=\pm3.46=\pm\sqrt{3}t_3$, the second is $E=\pm2.0=\pm t_3$, and the third is the zero-energy modes. The system also undergoes the topological phase transition at $t_1=\pm\sqrt{t_2^2+\gamma^2}=\pm1.12$. All three types of modes are presented in the region between these two phase transition points. From the probability density spectra of the wavefunction for different edge modes, we can also find that the three edge modes have different local properties. For the edge modes of $E=\pm3.464$ [see (i)], the left side $[a_{(1-5),1}]$ contributes to

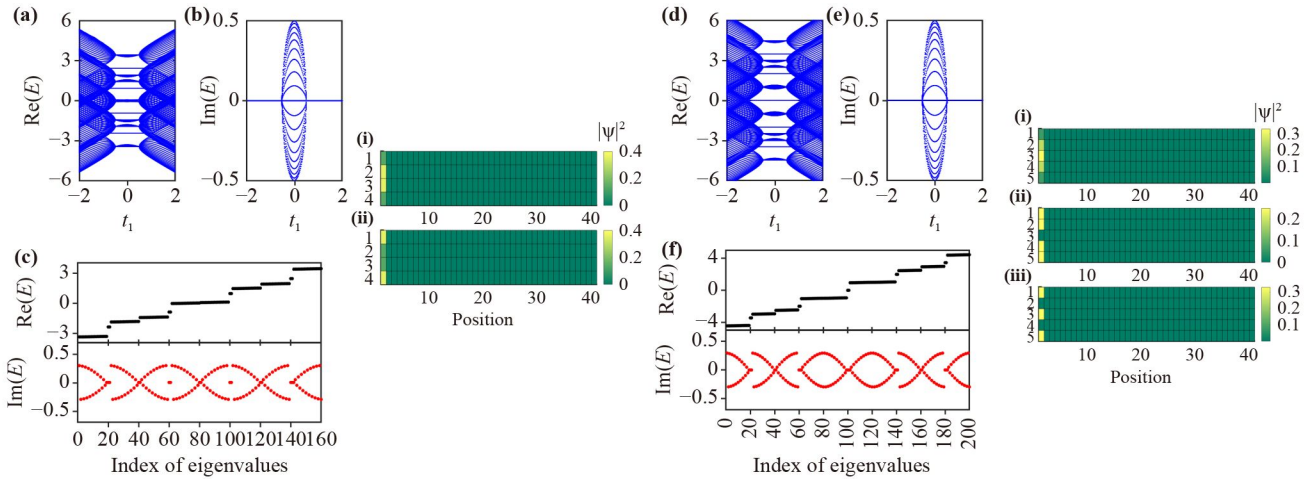

Fig. 7 **(a–c)** Eigenenergy and probability density spectra for $M = 4$ in the case of $t_3 = 1.5$. (a, b) Real and imaginary parts of energy. (c) Eigenenergy spectra of $t_1 = 0.4$. (i, ii) indicate the probability density spectra with two types of edge modes. **(d–f)** Eigenenergy and probability density spectra under the situation of $M = 5$ with $t_3 = 2.0$. (d, e) Real and imaginary parts of energy. (f) Eigenenergy of $t_1 = 0.4$. (i–iii) describe the probability density spectra with three types of edge modes. Other parameters are $t_2 = 1.0$ and $\gamma = 0.5$.

the localization of the system, but mainly in the sublattice $a_{3,1}$, followed by $a_{2,1}$ and $a_{4,1}$. For the edge modes of $E = \pm 2.0$ are mainly localized at sublattice $a_{1,1}$, $a_{2,1}$, $a_{4,1}$ and $a_{5,1}$, and the four positions contribute equally to the localization of the system. (iii) presents the wavefunctions of zero-energy modes, which are localized on the left side of the system, with probability distribution at sites of $a_{1,1}$, $a_{3,1}$ and $a_{5,1}$. Therefore, for the five-layer nonreciprocal structure, the system not only has twofold degenerate edge modes, but also has purely real energy zero-energy modes in the band gap.

Next we focus on the localization properties of bulk states in $M = 4$. Figure 8(a) corresponds to the eigenenergy spectra for $t_1 = 0.4$, and the color indicates the value of IPR. By judging the size of IPR, we observe that the IPR of the bulk states is approximately equal to $0.06 - 0.10$. The system has four-classes bulk bands. The right column (i)–(xii) show the probability density spectra with these four-classes bulk bands. It can be clearly found that the localization properties are different for these four-classes bulk bands. To be specific, the red arrow line represents the first-class bulk band with energy range of $E \in (\pm 3.45 \pm 0.30\mathrm{i} \sim \pm 3.38)$. We can find from (i)–(iii) that the system mainly displays localization in the middle two chains, $(a_{2,n}, b_{2,n})$ and $(a_{3,n}, b_{3,n})$. For the second-class bulk band (green arrow line) with energy range of $E \in (\pm 1.92 \pm 0.30\mathrm{i} \sim \pm 1.88)$, the localization is opposite to the first-class bulk band. They are mainly localized at the first and forth chains, $(a_{1,n}, b_{1,n})$ and $(a_{4,n}, b_{4,n})$. For the third-class bulk band of $E \in (\pm 1.43 \pm 0.30\mathrm{i} \sim \pm 1.48)$ with the purple arrow line, its localization properties are the same as the first-class bulk band. Finally, in the fourth-class bulk band $[E \in (\pm 0.07 \pm 0.30\mathrm{i} \sim \pm 0.02)]$, the wavefunction is mainly localized at the first and forth chains. This result is the same as the second-class bulk band.

At last, we discuss in detail the localization of the bulk states for $M = 5$. Figure 9 shows the eigenenergy spectra of $t_1 = 0.4$ and $\gamma = 0.5$. The color expresses the value of IPR. For the bulk bands, they can be divided into five classes, the first of which is the energy band with $E \in (\pm 4.46 \pm 0.30\mathrm{i} \sim \pm 4.41)$ [red arrow line]; the second class is the energy band of $E \in (\pm 3.00 \pm 0.30\mathrm{i} \sim \pm 2.95)$ [green arrow line]; the yellow arrow line represent the third-class bulk band with $E \in (\pm 2.47 \pm 0.30\mathrm{i} \sim \pm 2.52)$; the fourth- and fifth-class energy band respectively indicate the $E \in (\pm 1.00 \pm 0.30\mathrm{i} \sim \pm 1.05)$ and $E \in (\pm 0.99 \pm 0.30\mathrm{i} \sim \pm 0.95)$. The IPR values for the bulk states are approximately from $\mathrm{IPR} = 0.051$ to $\mathrm{IPR} = 0.11$. The figures (i)–(xv) display the probability density spectra of the five-classes bulk bands. We can clearly observe that similar to $M = 3$, the bulk states of $M = 5$ have "parity effect" in terms of locality. The local effects of the bulk bands can be distinguished into three main types. More specifically, in (i)–(iii) and (vii)–(ix), the first- and third-class bulk bands are mainly localized at the middle chain $(a_{3,n}, b_{3,n})$, and the nearest is $(a_{2,n}, b_{2,n})$ and $(a_{4,n}, b_{4,n})$. The (iv)–(vi) shows the wavefunction probability density of second-class bulk band, and the wavefunction is localized at the four chains of $[a_{1(5),n}, b_{1(5),n}]$ and $[a_{2(4),n}, b_{2(4),n}]$. Besides, these four chains have the same probability density intensity, however, the chain $(a_{3,n}, b_{3,n})$ is empty to occupy the state. The fourth-class bulk band has the same localization phenomena as the second-class, as shown in (x)–(xii). For the fifth-class bulk band, we can find the localization effect is better than other bands because the IPR is larger in Fig. 9(a). (xiii)–(xv) indicate

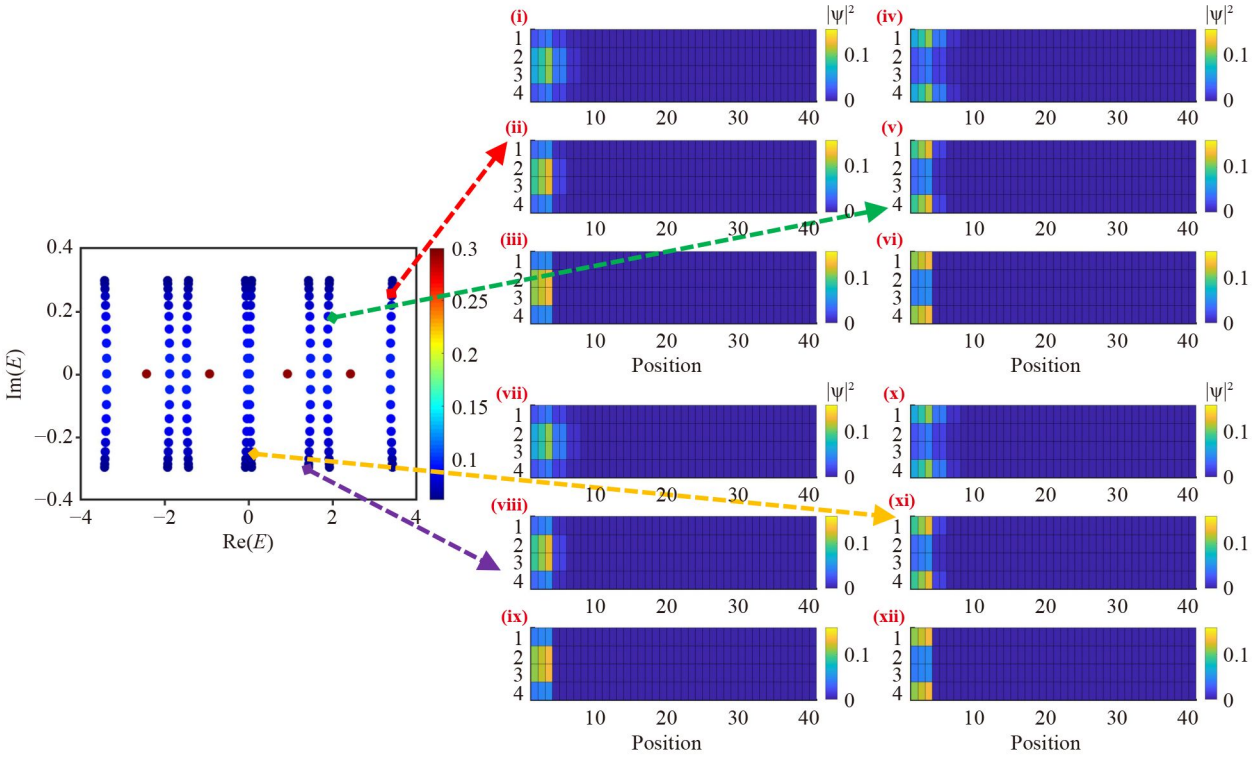

Fig. 8 Eigenenergy spectra for $M = 4$, where $\gamma = 0.5$. The colors represent the values of IPR. (i–xii) Probability density spectra of these four-classes bulk bands. Specifically, (i–iii) denote the localization probability density of $E = \pm 3.45 \pm 0.30\mathrm{i}$, $E = \pm 3.40 \pm 0.18\mathrm{i}$ and $E = \pm 3.38$, respectively; (iv–vi) respectively correspond to the cases of $E = \pm 1.92 \pm 0.30\mathrm{i}$, $E = \pm 1.90 \pm 0.18\mathrm{i}$ and $E = \pm 1.88$; (vii–ix) indicate the cases of $E = \pm 1.43 \pm 0.30\mathrm{i}$, $E = \pm 1.46 \pm 0.18\mathrm{i}$ and $E = \pm 1.48$; (x–xii) indicate the cases of $E = \pm 0.07 \pm 0.30\mathrm{i}$, $E = \pm 0.04 \pm 0.18\mathrm{i}$ and $E = \pm 0.02$, respectively. Other parameters are taken to be $t_1 = 0.4$, $t_2 = 1.0$, and $t_3 = 1.5$.

that the wavefunction probability density is mainly contributed by the odd chains $[(a_{1,n}, b_{1,n})$, $(a_{3,n}, b_{3,n})$, and $(a_{5,n}, b_{5,n})]$, whereas the even chains $[(a_{2,n}, b_{2,n})$ and $(a_{4,n}, b_{4,n})]$ show empty occupation. The probability density components of the three odd chains display the same magnitude.

Based on the results above, we know that the structures with different layers show common properties. The nonreciprocal coupling γ leads to the non-Hermitian skin effect, which changes some of the bulk states to be complex states. In addition, γ induces the topological phase transition in the system, and the twofold degenerate edge modes appear in the band gap. The increase of γ does not change the eigenenergy and localization of the edge modes, but induces the splitting of the edge modes. In particular, the increase of layer number of this SSH lattice take a significant modulating effect on the system properties. To better observe the changes in bulk states and edge modes, the details of the respective structures are shown in Table 2. We can anticipate that the increase of layer number has a small effect on the non-Hermitian skin effect, but plays nontrivial roles in modulating the number, energies and localization of edge modes and bulk states. Therefore, the whole system displays the "parity effect". To be specific, the first type of "parity effect" is manifested in the bulk states. In the "Localization" column, the color indicates the magnitude of the probability density. For the few-layer structures, i.e., $M = 1$ and $M = 2$, the localization of the bulk states does not show obvious "parity effect". However, for systems with $M \geq 3$, the localization of bulk states exhibits the clear "parity effect". Namely, for odd M, there are $(M+1)/2$-classes bulk bands with $(M+1)/2$ types of localities, and empty occupancy of the bulk states can be observed. Taking the case of $M = 3$ as an example, the first- and third-classes bulk bands are localized in the left boundary of the three chains, the second class is localized only in the first and third chains, and the probability density of the second chain is equal to 0. Alternatively, for the even M, the system has $M/2$-classes bulk bands, and the different classes of bulk bands have different localizations. The second type of "parity effect" is characterized by the edge modes. On one hand, when $M = 2, 4, \ldots$, we find that the system has only nonzero energy twofold degenerate edge modes which are localized at one side of the system. Otherwise, the whole system possesses purely real twofold degenerate zero-energy modes localized on one side of the system, in

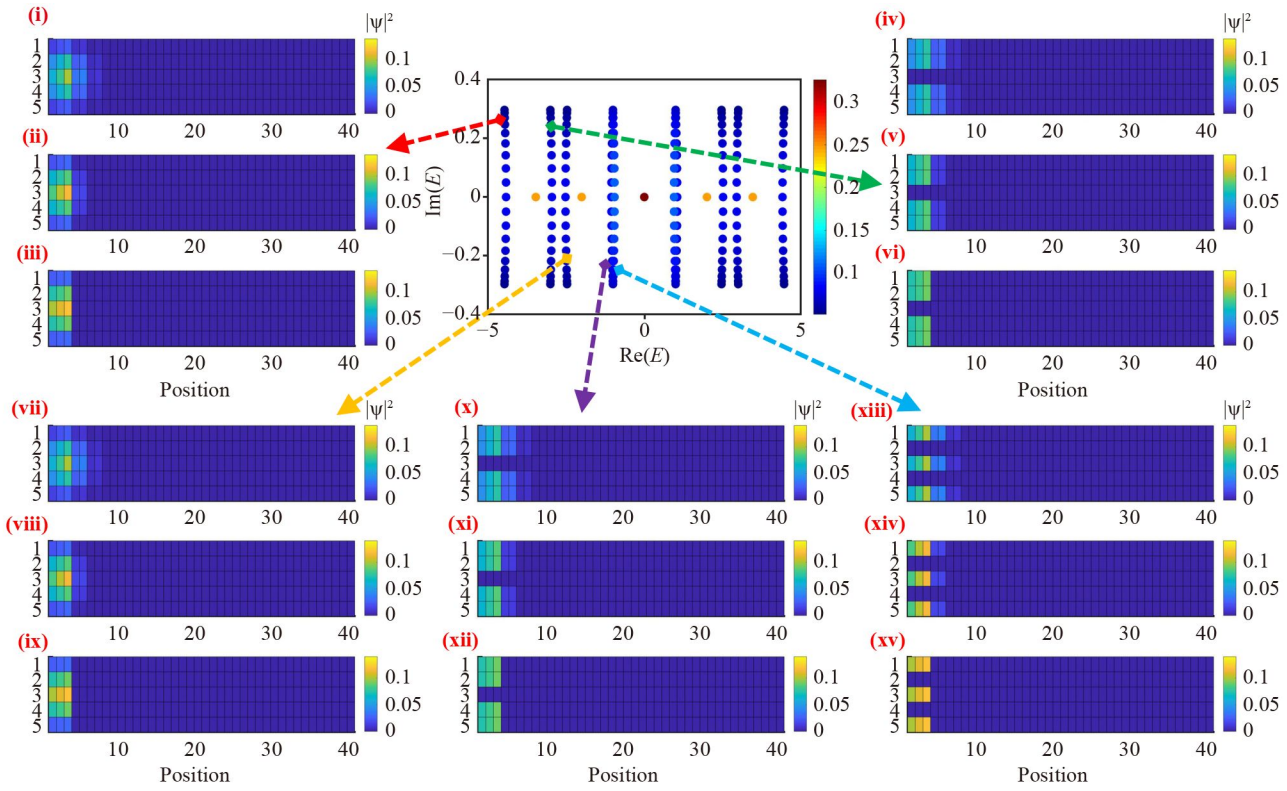

Fig. 9 Eigenenergy spectra of $M = 5$, under the condition of $\gamma = 0.5$. The colors represent the values of IPR. (i–xv) Probability density spectra of these five-classes bulk bands. To be specific, (i–iii) are the localization probability density of $E = \pm 4.46 \pm 0.30\mathrm{i}$, $E = \pm 4.43 \pm 0.18\mathrm{i}$, and $E = \pm 4.41$, respectively; (iv–vi) show the wavefunction probability density of $E = \pm 3.00 \pm 0.30\mathrm{i}$, $E = \pm 2.97 \pm 0.18\mathrm{i}$, and $E = \pm 2.95$; (vii–ix) mean the localization probability density of $E = \pm 2.47 \pm 0.30\mathrm{i}$, $E = \pm 2.50 \pm 0.18\mathrm{i}$, and $E = \pm 2.52$, respectively; (x–xii) stand for the cases of $E = \pm 1.00 \pm 0.30\mathrm{i}$, $E = \pm 1.03 \pm 0.18\mathrm{i}$, and $E = \pm 1.05$; (xiii–xv) indicate the probability density spectra of $E = \pm 0.99 \pm 0.30\mathrm{i}$, $E = \pm 0.97 \pm 0.18\mathrm{i}$, and $E = \pm 0.95$. Relevant parameters are taken to be $t_1 = 0.4$, $t_2 = 1.0$, $t_3 = 2.0$.

addition to the twofold degenerate nonzero-energy modes. Moreover, the zero-energy modes are better localized than the nonzero-energy modes.

3.4 Robustness to disorder

From the previous studies [76, 77], we understand that disorder usually plays an important role in changing the energy band structure of quantum systems, and meanwhile, robustness to disorder is a very important property of edge modes. Therefore, we would like to explore the changes in the eigenenergy spectrum due to the presence of disorder. Our main goal is to distinguish the robustness of different types of edge modes to disorder. In this work, we consider the case of off-diagonal disorder by respectively introducing disorder in the intercell hopping term t_2 and the interlayer coupling term t_3, i.e., $t_2' = t_2 + dw_n$ and $t_3' = t_3 + dw_n$, respectively, where n is the cell index, w_n is uniformly distributed between -1.0 and 1.0, and d is the disorder strength.

Figure 10 shows the real and imaginary parts of energy influenced by the increase of disorder strength d, in the case of disordered t_2. Figures 10 (a) and (b) represent the case of $t_1 = 0.4$ with $\gamma = 0.5$ in $M = 2$, and Figs. 10 (c) and (d) describe the case of $t_1 = 0.4$ with $\gamma = 0.5$ in $M = 3$. It is known that for the case of $M = 2$, the twofold degenerate edge modes with energy $E = \pm t_3$ exist in the band gap when $d = 0$, as shown in Fig. 3(a). Next as d increases, for the bulk states, the real part of energy becomes widened, while the imaginary part of the bulk states is gradually narrowed. For the edge modes, they undergo different changes in this process. When d is relatively small, the nonzero energy edge modes of this system are also robust. As the disorder strength increases, the twofold degenerate edge modes split. The energy of one split mode is fixed at $E = 1.0$, and the energy of the other split mode shows a decreasing trend. Subsequently, the edge modes are integrated into the body band following the further increase of disorder. Such splitting result indicates that the edge modes are not robust to disorder. Figure 10(c) and (d) show the results of $M = 3$ affected by disorder. When $d = 0$, the system has the twofold degenerate zero-energy modes as well as twofold degenerate edge modes with energy $E = \pm\sqrt{2}t_3$ [see Fig. 5(e)]. Next when d departs from its zero value, it can be observed that the variation of the

Table 2 Summary of non-Hermitian skin effect (NHSE), the number of edge modes (Pair), whether it is a zero-energy mode, robustness to disorder, and locality of bulk states and edge modes in this five types of structures. In the bulk bands, we present the probability density spectra of $\mathrm{Im}(E) = 0$. The lightness of the color indicates the magnitude of the probability density in the "Localization" column of bulk and edge modes.

Layers	Model	NHSE	Bulk states		Edge modes			
			Class	Localization	Pair	ZEM	Disorder	Localization
$M=1$		T	1	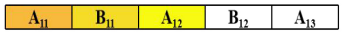	1	T	t_2, t_3	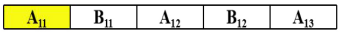
$M=2$	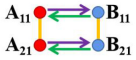	T	1(2)	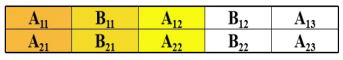	1	F	Weak t_2	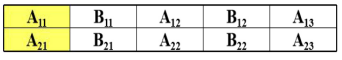
$M=3$	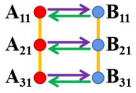	T	1(3)	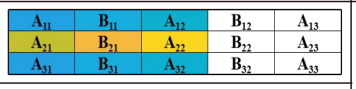	2	F	Weak t_2	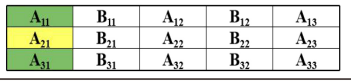
			2	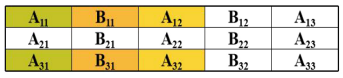		T	t_2, t_3	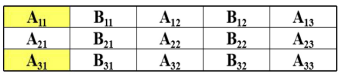
$M=4$	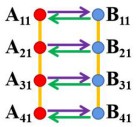	T	1(3)	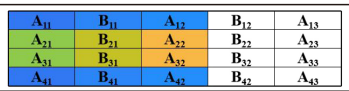	2	F	Weak t_2	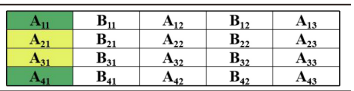
			2(4)	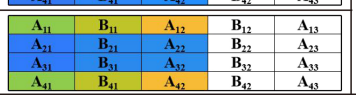		F		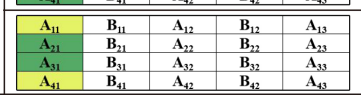
$M=5$	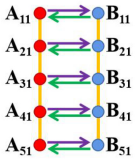	T	1(3)	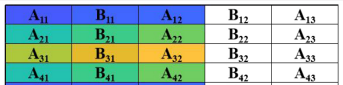	3	F	Weak t_2	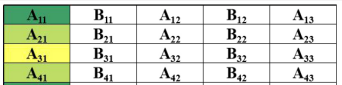
			2(4)	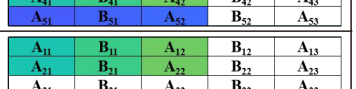		F		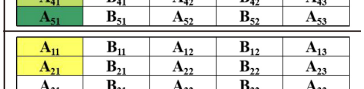
			5	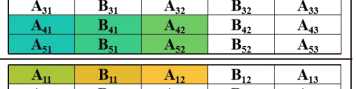		T	t_2, t_3	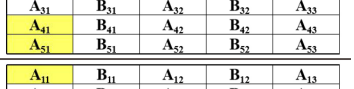

bulk states is similar to that of $M = 2$, but the two types of edge modes display different changes. To be specific, the nonzero edge modes also split with the increase of d, and then enter the bulk states at $d > 0.65$. Next, for the twofold degenerate zero-energy modes, we observe that the zero-energy modes do not split with the increase of disorder in the range $0 < d < 1.0$, whereas the zero-energy modes can exist in the larger range compared to the nonzero-energy modes. This indicates that zero-energy modes are better robust to disorder. As the disorder strength d continues to increase, the widening of the bulk band merges the zero-energy modes. Based on the above results, we find that the nonzero-energy edge modes for both $M = 2$ and $M = 3$ split more easily in the presence of disorder strength, whereas the twofold degenerate zero-energy modes are relatively robust. This means that disorder is a helpful mechanism in identifying the two types of edge modes.

To obtain a comprehensive understanding about the robustness of the edge modes, we next introduce off-diagonal disorder on the interlayer hopping term, i.e., $t_3' = t_3 + dw_n$. Figures 11(a)–(d) show the results when disorder is applied for the geometries of $M = 2$ and $M = 3$, where w_n is also uniformly distributed between -1.0 and 1.0. It can be noted that in this case, the bulk states still exhibit the tendency to be progressively wider as the disorder is enhanced. However, the effect of disorder on the edge modes is more pronounced. Specifically, for the case of $M = 2$, we find that as the disorder is introduced, the real part of the edge modes split into two. This result indicates that the edge modes can be affected easily by the disorder of t_3. When $M = 3$, the modulation effect of disorder on the edge modes is more apparent. As long as the disorder is not equal to zero, the original nonzero energy modes split directly into two modes and enter into the bulk states with the increase of the disorder. For zero energy modes, we can find that twofold degenerate zero-energy modes always exist in the range of $0 < d < 0.7$, and display robustness to the disorder of t_3. However, the widening of the bulk-state band leads to the survival of smaller gap in this system, resulting in the disappearance of the zero-energy modes. According to the above discussion, we can be sure that for $M = 2$ and $M = 3$, the nonzero energy edge modes are not robust to the disorder of t_3, whereas the zero-energy modes at $M = 3$ are more robust.

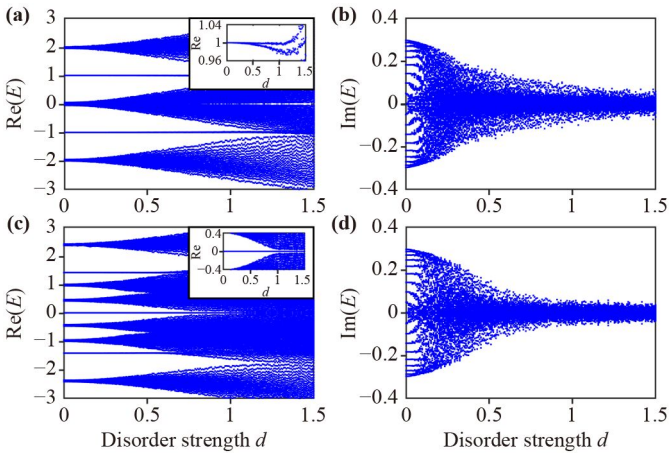

Fig. 10 **(a–d)** Energy spectra influenced by the different-strength disorder. The disorder is applied according to the manner of $t_2' = t_2 + dw_n$ with $w_n \in [-1.0, 1.0]$ and d is the disorder parameter. The parameters are set as (a) and (b) $t_1 = 0.4$, $\gamma = 0.5$ in $M = 2$, (c) and (d) $t_1 = 0.4$, $\gamma = 0.5$ in $M = 3$. The spectra are the average over 100 disorder results. Zoomed-in view of edge modes of $M = 2$ in (a) and zero-modes of $M = 3$ in (b), respectively.

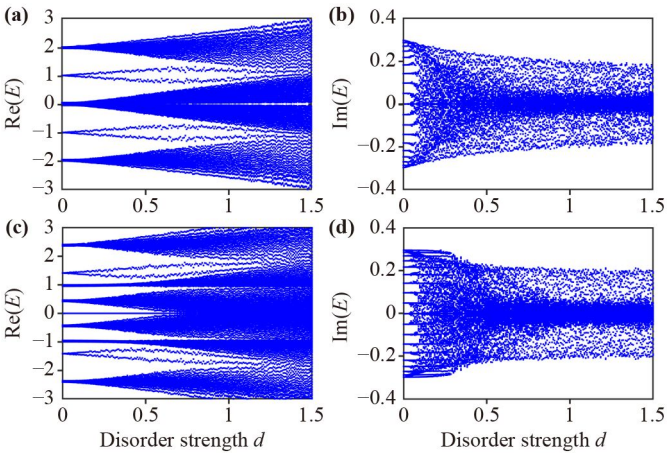

Fig. 11 **(a–d)** Energy spectra influenced by the different-strength disorder. The disorder is applied according to the manner of $t_3' = t_3 + dw_n$ with $w_n \in [-1.0, 1.0]$ and d is the disorder parameter. The parameters are set as (a) and (b) $t_1 = 0.4$, $\gamma = 0.5$ in $M = 2$, (c) and (d) $t_1 = 0.4$, $\gamma = 0.5$ in $M = 3$.

In view of the effects of the two disorders, we can clarify that regardless of odd or even M, nonzero energy modes are only weakly robust to weak disorder of t_2 and split directly at disorder of t_3 as long as $d \neq 0$. In contrast, zero-energy modes do not split for disordered t_2 and t_3 as the disorder strength increases, indicating better robustness to both disordered t_2 and t_3. We also understand that for odd-layer structures such as $M = 3, 5, \ldots$, the zero-energy modes can exist in the presence of disordered t_2, compared to the nonzero-energy modes. This phenomenon provides an alternative way for distinguishing the different types of edge modes.

4 Summary

To summarize, in this work we have performed investigations on the skin effects and topological properties in the multilayer non-Hermitian SSH structure, by taking into account the nonreciprocal intra-cell couplings in each layer. The calculation results show that in this system, the skin effects induced by nonreciprocal coupling display the apparent parity effect, following the increase of the layer number of this SSH structure. Namely in this system, the skin effects and topological phase transitions induced by nonreciprocal couplings display the apparent parity effect, following the increase of the layer number of this SSH structure. On the one hand, the skin effect is determined by the parity of the layer number of this SSH system, as well as the parity of the band index of the bulk state. On the other hand, for the topological edge modes, such an interesting parity effect can also be observed clearly. Furthermore, nonzero-energy edge modes and zero-energy edge modes show different variations in the presence of disorder, and zero-energy modes in the odd-layer structures are more robust to disorder, in comparison with the nonzero-energy edge modes in the other cases. Based on the obtained results, it can be thus believed that all these findings promote to understand the influences of nonreciprocal couplings on the types and properties of respective states in the SSH lattices.

Declarations The authors declare that they have no competing interests and there are no conflicts.

Acknowledgements This work was financially supported by the LiaoNing Revitalization Talents Program (Grant No. XLYC1907033), the National Natural Science Foundation of China (Grant No. 11905027), the Natural Science Foundation of Liaoning province (Grant No. 2023-MS-072), and Fundamental Research Funds for the Central Universities of Ministry of Education of China (Grant Nos. N2209005 and N2205015).

References

1. C. M. Bender, D. C. Brody, and H. F. Jones, Complex extension of quantum mechanics, *Phys. Rev. Lett.* 89, 270401 (2002)
2. V. V. Konotop, J. Yang, and D. A. Zezyulin, Non-linear waves in *PT*-symmetric systems, *Rev. Mod. Phys.* 88, 035002 (2016)
3. Y. Ashida, Z. Gong, and M. Ueda, Non-Hermitian physics, *Adv. Phys.* 69, 249 (2020)
4. S. K. Özdemir, S. Rotter, F. Nori, and L. Yang, Parity–time symmetry and exceptional points in

photonics, *Nat. Mater.* 18, 783 (2019)
5. C. Wu, N. Liu, G. Chen, and S. Jia, Non-Hermiticity-induced topological transitions in long-range Su–Schrieffer–Heeger models, *Phys. Rev. A* 106, 012211 (2022)
6. A. Fan and S. D. Liang, Complex energy plane and topological invariant in non-Hermitian systems, *Front. Phys.* 17, 33501 (2022)
7. J. C. Budich and E. J. Bergholtz, Non-Hermitian topological sensors, *Phys. Rev. Lett.* 125, 180403 (2020)
8. F. Koch and J. C. Budich, Quantum non-Hermitian topological sensors, *Phys. Rev. Research* 4, 013113 (2022)
9. A. McDonald and A. A. Clerk, Exponentially-enhanced quantum sensing with non-Hermitian lattice dynamics, *Nat. Commun.* 11, 5382 (2020)
10. M. Parto, S. Wittek, H. Hodaei, G. Harari, et al, Edge-mode lasing in 1D topological active arrays, *Phys. Rev. Lett.* 120, 113901 (2018)
11. S. Weidemann, M. Kremer, T. Helbig, T. Hofmann, et al., Topological funneling of light, *Science* 368, 311 (2020)
12. S. Garmon and K. Noba, Reservoir-assisted symmetry breaking and coalesced zero-energy modes in an open *PT*-symmetric Su–Schrieffer–Heeger model, *Phys. Rev. A* 104, 062215 (2021)
13. J.-R. Li, L.-L. Zhang, W.-B. Cui, and W.-J. Gong, Topological properties in non-Hermitian tetratomic Su–Schrieffer–Heeger lattices, *Phys. Rev. Research* 4, 023009 (2022)
14. A. Yoshida, Y. Otaki, R. Otaki, and T. Fukui, Edge states, corner states, and flat bands in a two-dimensional *PT*-symmetric system, *Phys. Rev. B* 100, 125125 (2019)
15. A. F. Tzortzakakis, A. Katsaris, N. E. Palaiodi-mopoulos, P. A. Kalozoumis, et al., Topological edge states of the *PT*-symmetric Su–Schrieffer–Heeger model: An effective two-state description, *Phys. Rev. A* 106, 023513 (2022)
16. X. Zhu, H. Wang, S. K. Gupta, H. Zhang, B. Xie, M. Lu, and Y. Chen, Photonic non-Hermitian skin effect and non-Bloch bulk–boundary correspondence, *Phys. Rev. Research* 2, 013280 (2020)
17. K. Xu, X. Zhang, K. Luo, R. Yu, D. Li, and H. Zhang, Coexistence of topological edge states and skin effects in the non-Hermitian Su–Schrieffer–Heeger model with long-range nonreciprocal hopping in topoelectric realizations, *Phys. Rev. B* 103, 125411 (2021)
18. S. M. Rafi-Ul-Islam, B. S. Zhuo, S. Haydar, C. H. Lee, and M. B. A. Jalil, Critical hybridization of skin modes in coupled non-Hermitian chains, *Phys. Rev. Research* 4, 013243 (2022)
19. R. Lin, T. Tai, L. Li, and C. H. Lee, Topological non-Hermitian skin effect, *Front. Phys.* 18, 53605 (2023)
20. C. M. Bender, and S. Boettcher, Real spectra in non-Hermitian Hamiltonians having *PT* symmetry, *Phys. Rev. Lett.* 80, 5243 (1998)
21. C. M. Bender, Making sense of non-Hermitian Hamiltonians, *Rep. Prog. Phys.* 70, 947 (2007)
22. S. Longhi, Convective and absolute *PT*-symmetry breaking in tight-binding lattices, *Phys. Rev. A* 88, 052102 (2013)
23. F. K. Kunst, E. Edvardsson, J. C. Budich, and E. J. Bergholtz, Biorthogonal bulk–boundary correspondence in non-Hermitian systems, *Phys. Rev. Lett.* 121, 026808 (2018)
24. L. Jin, P. Wang, and Z. Song, Su–Schrieffer–Heeger chain with one pair of *PT*-symmetric defects, *Sci. Rep.* 7, 5903 (2017)
25. Y. Xing, L. Qi, J. Cao, D. Y. Wang, C. H. Bai, H. F. Wang, A. D. Zhu, and S. Zhang, Spontaneous *PT*-symmetry breaking in non-Hermitian coupled-cavity array, *Phys. Rev. A* 96, 043810 (2017)
26. X. S. Li, Z. Z. Li, L. L. Zhang, and W. J. Gong, *PT* symmetry of the Su–Schrieffer–Heeger model with imaginary boundary potentials and next-nearest-neighboring coupling, *J. Phys. Condens. Matter* 32, 165401 (2020)
27. K. Kawabata, Y. Ashida, H. Katsura, and M. Ueda, Parity–time-symmetric topological superconductor, *Phys. Rev. B* 98, 085116 (2018)
28. M. Klett, H. Cartarius, D. Dast, J. Main, and G. Wunner, Relation between *PT*-symmetry breaking and topologically nontrivial phases in the Su–Schrieffer–Heeger and Kitaev models, *Phys. Rev. A* 95, 053626 (2017)
29. L. Jin, Topological phases and edge states in a non-Hermitian trimerized optical lattice, *Phys. Rev. A* 96, 032103 (2017)
30. L. L. Zhang, J. R. Li, D. Zhang, T. T. Xu, W. B. Cui, and W. J. Gong, *PT*-symmetric non-Hermitian zigzag-edged ribbon of bilayer photonic graphene, *Results in Physics* 34, 105274 (2022)
31. X. M. Zhao, C. X. Guo, S. P. Kou, L. Zhuang, and W. M. Liu, Defective Majorana zero modes in a non-Hermitian Kitaev chain, *Phys. Rev. B* 104, 205131 (2021)
32. C. Yuce and H. Ramezani, Topological states in a non-Hermitian two-dimensional Su–Schrieffer–Heeger model, *Phys. Rev. A* 100, 032102 (2019)
33. L. Feng, R. El-Ganainy, and L. Ge, Non-Hermitian photonics based on parity–time symmetry, *Nature Photon.* 11, 752 (2017)
34. A. Regensburger, C. Bersch, M. A. Miri, G. Onishchukov, D. N. Christodoulides, and U. Peschel, Parity–time synthetic photonic lattices, *Nature* 488, 167 (2012)
35. Y. Wu, B. Zhu, S. F. Hu, et al., Floquet control of the gain and loss in a *PT*-symmetric optical coupler, *Front. Phys.* 12, 121102 (2017)
36. C. Chen, Y. Liu, L. Zhao, et al., Asymmetric nonlinear-mode-conversion in an optical waveguide with *PT* symmetry, *Front. Phys.* 17, 52504 (2022)
37. A. Stegmaier, S. Imhof, T. Helbig, T. Hofmann, C. H. Lee, M. Kremer, A. Fritzsche, et al., Topological defect engineering and *PT* symmetry in non-Hermitian electrical circuits, *Phys. Rev. Lett.* 126, 215302 (2021)
38. Z. Lin, J. Schindler, F. M. Ellis, T. Kottos, Experimental observation of the dual behavior of *PT*-symmetric scattering, *Phys. Rev. A* 85, 050101(R) (2012)
39. L. Lu, J. D. Joannopoulos, and M. Soljăcić, Topological photonics, *Nature Photon.* 8, 821 (2014)
40. M. G. Silveirinha, Topological theory of non-Hermitian photonic systems, *Phys. Rev. B* 99, 125155 (2019)
41. T. Ozawa, H. M. Price, A. Amo, N. Goldman, M. Hafezi, L. Lu, M. C. Rechtsman, D. Schuster, J. Simon,

O. Zilberberg, and I. Carusotto, Topological photonics, *Rev. Mod. Phys.* 91, 015006 (2019)
42. G. Q. Liang and Y. D. Chong, Optical resonator analog of a two-dimensional topological insulator, *Phys. Rev. Lett.* 110, 203904 (2013)
43. H. Hodaei, M. A. Miri, A. U. Hassan, W. E. Hayenga, M. Heinrich, D. N. Christodoulides, et al., Single mode lasing in transversely multi-moded *PT*-symmetric microring resonators, *Laser Photonics Rev.* 10, 494 (2016)
44. Y. Y. Fu, Y. Fei, D. X. Dong, et al., Photonic spin Hall effect in *PT* symmetric metamaterials, *Front. Phys.* 14, 62601 (2019)
45. M. Kang, F. Liu, and J. Li, Effective spontaneous *PT*-symmetry breaking in hybridized metamaterials, *Phys. Rev. A* 87, 053824 (2013)
46. Y. Sun, W. Tan, H. Q. Li, J. Li, and H. Chen, Experimental demonstration of a coherent perfect absorber with *PT* phase transition, *Phys. Rev. Lett.* 112, 143903 (2014)
47. H. Jing, S. K. Ozdemir, X. Y. Lü, J. Zhang, L. Yang, and F. Nori, *PT*-symmetric phonon laser, *Phys. Rev. Lett.* 113, 053604 (2014)
48. Y. D. Chong, L. Ge, and A. D. Stone, *PT*-symmetry breaking and laser-absorber modes in optical scattering systems, *Phys. Rev. Lett.* 106, 093902 (2011)
49. S. Yao, and Z. Wang, Edge states and topological invariants of non-Hermitian systems, *Phys. Rev. Lett.* 121, 086803 (2018)
50. S. Yao, F. Song, and Z. Wang, Non-Hermitian Chern bands, *Phys. Rev. Lett.* 121, 136802 (2018)
51. V. M. Martinez Alvarez, J. E. Barrios Vargas, L. E. F. Foa Torres, Non-Hermitian robust edge states in one dimension: Anomalous localization and eigenspace condensation at exceptional points, *Phys. Rev. B* 97, 121401(R) (2018)
52. C. H. Lee and R. Thomale, Anatomy of skin modes and topology in non-Hermitian systems, *Phys. Rev. B* 99, 201103 (2019)
53. S. Weidemann, M. Kremer, T. Helbig, T. Hofmann, A. Stegmaier, M. Greiter, R. Thomale, and A. Szameit, Topological funneling of light, *Science* 19, 311 (2020)
54. Y. Xiong, Why does bulk boundary correspondence fail in some non-Hermitian topological models, *J. Phys. Commun.* 2, 035043 (2018)
55. T. S. Deng and W. Yi, Non-Bloch topological invariants in a non-Hermitian domain wall system, *Phys. Rev. B* 100, 035102 (2019)
56. F. Song, S. Yao, and Z. Wang, Non-Hermitian topological invariants in real space, *Phys. Rev. Lett.* 123, 246801 (2019)
57. K. Yokomizo and S. Murakami, Non-Bloch band theory of non-Hermitian systems, *Phys. Rev. Lett.* 123, 066404 (2019)
58. L. Xiao, T. S. Deng, K. K. Wang, G. Y. Zhu, Z. Wang, W. Yi, and P. Xue, Observation of non-Hermitian bulk–boundary correspondence in quantum dynamics, *Nat. Phys.* 16, 761 (2020)
59. P. C. Cao, Y. G. Peng, Y. Li, and X. F. Zhu, Phase-locking diffusive skin effect, *Chin. Phys. Lett.* 39, 057801 (2022)
60. A. Ghatak, M. Brandenbourger, J. van Wezel, and C. Coulais, Observation of non-Hermitian topology and its bulk–edge correspondence in an active mechanical metamaterial, *Proc. Natl. Acad. Sci.* 117, 29561 (2020)
61. E. J. Bergholtz, J. C. Budich, and F. K. Kunst, Exceptional topology of non-Hermitian systems, *Rev. Mod. Phys.* 93, 015005 (2021)
62. T. Helbig, T. Hofmann, S. Imhof, M. Abdelghany, T. Kiessling, L. W. Molenkamp, C. H. Lee, A. Szameit, M. Greiter, and R. Thomale, Chiral voltage propagation and calibration in a topolectrical Chern circuit, *Nat. Phys.* 16, 747 (2020)
63. L. Xie, L. Jin, and Zhi Song, Antihelical edge states in two-dimensional photonic topological metals, *Sci. Bull.* 68, 255 (2023)
64. K. Kawabata, K. Shiozaki, M. Ueda, and M. Sato, Symmetry and topology in non-Hermitian physics, *Phys. Rev. X* 9, 041015 (2019)
65. Z. P. Gong, Y. Ashida, K. Kawabata, K. Takasan, S. Higashikawa, and M. Ueda, Topological phases of non-Hermitian systems, *Phys. Rev. X* 8, 031079 (2018)
66. K. Takata and M. Notomi, Photonic topological insulating phase induced solely by gain and loss, *Phy. Rev. Lett.* 121, 213902 (2018)
67. H. C. Wu, L. Jin, and Z. Song, Topology of an anti-parity–time symmetric non-Hermitian Su–Schrieffer–Heeger model, *Phys. Rev. B* 103, 235110 (2021)
68. T. S. Deng and W. Yi, Non-Bloch topological invariants in a non-Hermitian domain wall system, *Phys. Rev. B* 100, 035102 (2019)
69. C. X. Guo, C. H. Liu, X. M. Zhao, Y. Liu, and S. Chen, Exact solution of non-Hermitian systems with generalized boundary conditions: Size-dependent boundary effect and fragility of the skin effect, *Phys. Rev. Lett.* 127, 116801 (2021)
70. J. R. Li, C. Luo, L. L. Zhang, S. F. Zhang, P. P. Zhu, and W. J. Gong, Band structures and skin effects of coupled nonreciprocal Su–Schrieffer–Heeger lattices, *Phys. Rev. A* 107, 022222 (2023)
71. Y. X. Liu, Y. C. Wang, X. J. Liu, Q. Zhou, and S. Chen, Exact mobility edges, *PT*-symmetry breaking, and skin effect in one-dimensional non-Hermitian quasicrystals, *Phys. Rev. B* 103, 014203 (2021)
72. L. J. Zhai, G. Y. Huang, and S. Yin, Cascade of the delocalization transition in a non-Hermitian interpolating Aubry–André–Fibonacci chain, *Phys. Rev. B* 104, 014202 (2021)
73. C. Mejia-Cortes and M. I. Molina, Interplay of disorder and *PT* symmetry in one-dimensional optical lattices, *Phys. Rev. A* 91, 033815 (2015)
74. L. Jin and Z. Song, Bulk–boundary correspondence in a non-Hermitian system in one dimension with chiral inversion symmetry, *Phys. Rev. B* 99, 081103(R) (2019)
75. F. Evers and A. D. Mirlin, Fluctuations of the inverse participation ratio at the Anderson transition, *Phys. Rev. Lett.* 84, 3690 (2000)
76. V. M. M. Alvarez, and M. D. Coutinho-Filho, Edge states in trimer lattices, *Phys. Rev. A* 99, 013833 (2019)
77. T. E. Lee, Anomalous edge state in a non-Hermitian lattice, *Phys. Rev. Lett.* 116, 133903 (2016)